MODELING OF ENVIRONMENTAL TEMPERATURE DEPENDENCY FOR SENSORS OPERATED BY SAGNAC EFFECT

A THESIS SUBMITTED TO
THE GRADUATE SCHOOL OF NATURAL AND APPLIED SCIENCES
OF
MIDDLE EAST TECHNICAL UNIVERSITY

BY

ECE ALAÇAKIR

IN PARTIAL FULFILLMENT OF THE REQUIREMENTS
FOR
THE DEGREE OF MASTER OF SCIENCE
IN
PHYSICS

FEBRUARY 2019

Approval of the thesis:

MODELING OF ENVIRONMENTAL TEMPERATURE DEPENDENCY FOR SENSORS OPERATED BY SAGNAC EFFECT

submitted by **ECE ALAÇAKIR** in partial fulfillment of the requirements for the degree of **Master of Science in Physics Department, Middle East Technical University** by,

Prof. Dr. Halil Kalıpçılar
Dean, Graduate School of **Natural and Applied Sciences** _____

Prof. Dr. Altuğ Özpineci
Head of Department, **Physics** _____

Assoc. Prof. Dr. Serhat Çakır
Supervisor, **Physics, METU** _____

Examining Committee Members:

Assoc. Prof. Dr. Hüseyin Oymak
Physics, Atılım University _____

Assoc. Prof. Dr. Serhat Çakır
Physics, METU _____

Prof. Dr. İsmail Rafatov
Physics, METU _____

Date: 18.02.2019

I hereby declare that all information in this document has been obtained and presented in accordance with academic rules and ethical conduct. I also declare that, as required by these rules and conduct, I have fully cited and referenced all material and results that are not original to this work.

Name, Surname: Ece Alaçakır

Signature:

ABSTRACT

MODELING OF ENVIRONMENTAL TEMPERATURE DEPENDENCY FOR SENSORS OPERATED BY SAGNAC EFFECT

Alaçakır, Ece
Master of Science, Physics
Supervisor: Assoc. Prof. Dr. Serhat Çakır

February 2019, 97 pages

In this thesis, the purpose is that theoretical, experimental and simulation environment are combined to observe and model the thermal sensitivity of a gyroscope which is operated by the principle of Sagnac effect. It is essential to enhance the knowledge and experience, and to gain ability to simulate for different thermal conditions for future developments of the advanced gyroscope technologies. This thesis investigates how external temperature change influences the performance of fiber optic gyroscopes, which are purchased in line with the possibilities, theoretically, experimentally and in simulation model. Thus, deviations in rotation rate errors are observed in the measurement of the performance parameters of the gyroscopes subjected to the tests at different thermal profiles. A model is created by supporting with theoretical values, and simulations are prepared in a computer environment

Keywords: Optical Gyroscopes, Temperature Dependency, Shupe Effect, Tdot Effect, Elasto-optic Effect

ÖZ

ÇEVRESEL SICAKLIK DEĞİŞİMİNİN SAGNAC ETKİLİ ALGILAYICI HATALARINA ETKİSİNİN MODELLEMESİ

Alaçakır, Ece
Yüksek Lisans, Fizik
Tez Danışmanı: Doç. Dr. Serhat Çakır

Şubat 2019, 97 sayfa

Bu tezde; teorik, deney ve benzetim yöntemleri kullanılarak, Sagnac etkisi prensibi ile çalışan bir optik dönüölçerin ısıl duyarlılığının gözlemlenmesi ve etkilerinin modellenmesi amaçlanmıştır. Gelecekteki çalışmalarda kullanılmak üzere, gelişmiş dönüölçer teknolojileri hakkında bilgi birikiminin ve deneyimin arttırtılması ve bilgisayar ortamında farklı sınır koşulları altında modelleme yapılabilmesi önem taşımaktadır. Bu tez; dış sıcaklık değişiminin, imkanlar doğrultusunda satın alınmış bir fiber optik dönüölçerin performansını nasıl etkilediğini araştırmaktadır. Farklı dış sıcaklıklarda testlere tabii tutulan dönüölçerin performans parametrelerinin ölçümlerinde sapmalar gözlemlenmiştir. Teorik değerler ve bilgisayar ortamında hazırlanan benzetim ile desteklenerek bir model oluşturulmuştur.

Anahtar Kelimeler: Optik Dönüölçerler, Sıcaklık Bağımlılığı, Shupe Etkisi, Tdot Etkisi, Elasto-Optik Etkisi

To My Dear Family

ACKNOWLEDGMENTS

I wish to express my sincere gratitude to my supervisor Assoc. Prof. Dr. Serhat Çakır for his patience, guidance, advice, encouragements and motivation.

I would like to express my profound gratitude to my mother, father and little sister for my years of study and for providing me with endless support during writing of this thesis.

Moreover, I would like to thank my friends Pelin Cabadağ, Merve Akkaya, Feriha Ceren Alkan, Ece Kuyululu, İpek Düzgören, Hanife Usta, Selva Sargın Güçlü, Aslı Doğan who always helps me to overcome my daily life problems easily. They each are precious and esteemed people in my life.

This study was supported by Roketsan A.S. I am very grateful to stuffs who provide me with the opportunity to be able to perform tests in the laboratory.

Finally, I express my love and thanks to my dear fiance Yunus Demir for providing me continuous motivation and for always supporting me. He always has faith in my success.

TABLE OF CONTENTS

LIST OF TABLES

TABLES

LIST OF FIGURES

FIGURES

LIST OF ABBREVIATIONS

ABBREVIATIONS

AOFS	Acoustic Optic Frequency Shifter
AOM	Acousto-optic modulator
ARW	Angle Random Walk
BFOG	Brillioun Fiber Optic Gyroscope
CCW	Counter Clock-wise
CW	Clock-wise
DOF	Degree of Freedom
DTG	Dynamically Tuned Gyroscope
EDFS	Er-Doped Fiber Source
ESG	Electrostatic Gyroscope
FOG	Fiber Optic Gyroscope
I/O	Input/Output
IFOG	Interferometric Fiber Optic Gyroscope
MEMS	Micro-Electro-Mechanical Systems
MIOC	Micro Integrated Optic Chip
NMR	Nuclear Magnetic Resonance
ppm	Parts per million
RFOG	Resonant Fiber Optic Gyroscope
RLG	Ring Laser Gyroscope
SF	Scale Factor
SLD	Super Luminescence Diode
TIR	Total Internal Reflection

LIST OF SYMBOLS

SYMBOLS

n_{SiO2}	Refractive index of silica
D_i	The diffusion coefficient
$E_{coating}$	Young's modulus of fiber coating
E_{core}	Young's modulus of fiber core
P_a	Axial stress
P_r	Radial stress
$\dot{T}$	Tdot- Rate of change of temperature in time
a_{11} and a_{12}	Photo-elastic coefficients
$\frac{dn_{SiO2}}{dT}$	Thermal dependence of Silica refractive index
k_b	Boltzman constant
q_h	Heat flow vector
Ω_E	Rotation rate error
α_{SiO2}	Thermal expansion coefficient of silica
α_c	Thermal expansion coefficient of fiber coating
ε_0	Vacuum permittivity
$\Delta\varphi$	Phase difference
A	Area of a circular path
c	Speed of light
C	The concentration of diffusing material
d_c	Diameter of cladding
E_c	The local electric field
F_c	Coriolis force
L	Length of the fiber
m	Mass

M	The number of layer
n	Refractive index
N	The number of loop
r	Radius of a circular path
R	Inner coil diameter
s	The distance from fiber to end of adhesive material
t_{ccw}	Transit time for counter-clockwise beam
t_{cw}	Transit time for clockwise beam
x	The space coordinate which is measured normal to the area
ΔL_{CW}	The path that CW beam propagates
ΔL_{CcW}	The path that CCW beam propagates
ω	Angular rate
D	The average diameter of fiber coil
K	Thermal conductivity
N	The average number density of the Si–O bonds along the direction of the local electric field
R	The rate of heat transfer
T	Temperature
a	Polarizability
b	The volume energy density
l	Infinitesimal length
q	Electric charge
t	Time
v	Linear velocity
λ	Wavelength
μ	Poisson's coefficient
ρ	The density of the material
φ	Phase shift

CHAPTER 1

INTRODUCTION

The technology of control and guidance of the system is becoming very significant and needed in today's world due to knowing the position and the precession motion. The developments of the navigation technology are growing fast by means of researches and investigations about the physical theory and structural behavior of a system. Improving know-how about reasons and solutions of defects in a system, theoretical relations of concepts and observations not only in the real world, but also in the virtual environment leads to new and advance future technological developments.

The attitude and the trajectory of any vehicle are calculated by mathematical integration of acceleration and angular rate measurements when taking into account the initial orientation and position. There are sensors that use different principles of operation technique to detect the rotation rate, called gyroscopes.

In literature, there are many architectures, design techniques and fabrication technology of gyroscopes. In modern navigation systems, the gyroscopes have an important role in order to arrange, diagnose and control the movement of a vehicle from one place to another.

Gyroscope technology is being advanced day by day considering comprehension of its theory, mathematics and progression in the accomplishment of errors which can be resulted by environmental factors such as temperature change, vibration, shock, acoustic and magnetic effects.

When considered the optical (interferometric) gyroscopes, the temperature is one of the most significant errors which cause parasitic effects that decrease in the performance of the system (Lefevre, 2014).

Temperature transience error in fiber optic gyroscopes known as Shupe effect and its relation to temperature-induced stresses in the coil are critic occurrence of FOG technology (Lefevre, 2014).

In this thesis, the performance of a fiber optic gyroscope, which is purchased in line with the possibilities, is observed and examined under different external temperatures. Deviations which result from thermal changes have been observed in the measurement of some performance parameters of the gyroscope subjected to the tests. A model is built by supporting with theoretical values and simulations created on the computer environment. In the discussion and conclusion part, all these values and model are compared.

As a result, future researches are aimed to fully understand the physical theories, error sources and behaviors of errors for optical gyroscopes in order to eliminate and compensate them. After all, trends will be disposed to upgrade the gyroscope technology.

1.1. Gyroscope Technology and Applications in the World

A gyroscope is a device used for measuring orientation and angular velocity in a rotating frame (Armenise, 2014). Nowadays, rapidly developing gyroscope technology is used for sensing rotation rate of a system on land, sea, air and also space applications. Its wide spectrum of application area consists of military industry, automotive, medicine, space engineering, aeronautical and so on (Passaro, Cuccovillo, Vaiani, Carlo, & Campanella, 2017).

There are different classes of gyroscopes according to their performances, operating environment and their operating physical theory. Considering specific applications, gyroscopes can be produced in distinct performance grades with different physical theories and costs. Gyroscope costs and performance grades are directly related to the application requirements.

Therefore, gyroscope technology can be categorized as their variation in terms of their operating physical principles and commercial architectures. The classes of gyroscopes are as shown in Figure 1.1 (Passaro, Cuccovillo, Vaiani, Carlo, & Campanella, 2017) (Titterton & Weston, 2004) (Groves, 2008).

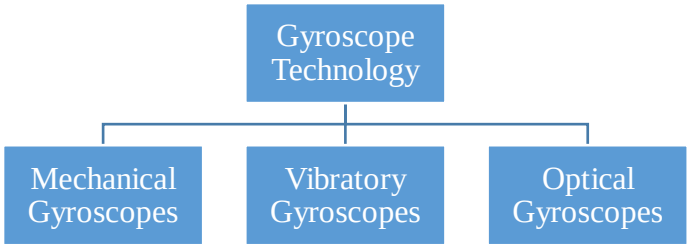

Figure 1.1. Types of GyroscopesTypes of GyroscopesTypes of Gyroscopes

In addition to gyroscope technology, there are many other types of conventional and unconventional gyroscopes mentioned in the heading of 1.2 that are not categorized in this way because the categorized gyroscope technologies which are more producible with today's technology and have wider application in industry.

1.1.1. Mechanical Gyroscopes

In 1852, the mechanical gyroscopes were first invented by physicist Leon Foucault during his researches of the Earth's rotation (Passaro, Cuccovillo, Vaiani, Carlo, & Campanella, 2017). The physical phenomenon of mechanical gyroscopes governs gyroscopic effect, which is based on the principles of conservation of angular momentum. This kind of gyroscopes is known as conventional gyroscopes.

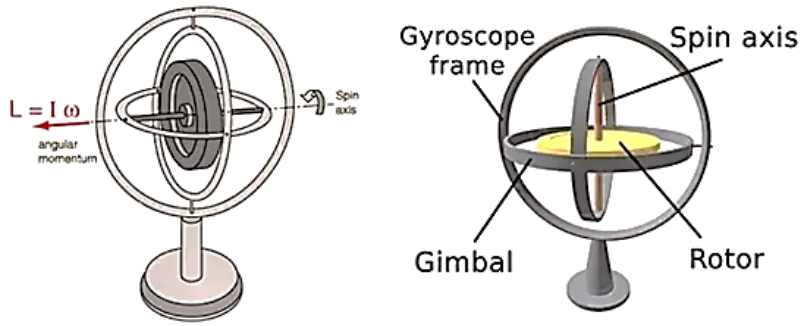

Figure 1.2 Illustration of a mechanical gyroscope *(Gyroscopic Effect, 2018)*

As shown in Figure 1.2, mechanical gyroscopes consist of a spinning wheel called rotor supported by a pair of gimbal which allows the spinning wheel to rotate in three axes. This wheel freely spins any orientation according to both of the axis perpendicular to its rotating axis (Woodman, 2007). If its parts are requested to be moved, the mechanism resists the motion. This resistance for the change in the direction of the rotation axis is called the gyroscopic effect (Groves, 2008).

The performance of the mechanical gyroscopes can be achieved to error rates of less than 0.00l°/h which is very precise value, and many devices of them are able to measure up to 500°/h (Titterton & Weston, 2004). Because the principle of this technology has been studying for a long time, rugged designs of mechanical gyroscopes are used in harsh environments such as military application and marine systems.

The traditional mechanical gyroscopes can be interpreted as macro-scale gyroscopes when compared to the newly developed gyroscopes up to micro dimensions. The main disadvantage of mechanical gyroscopes is that there are moving parts, which give rise to friction during rotation in the system that causes building on error. Using some friction reducing materials is also expensive (Woodman, 2007).

Spinning mass gyroscope, rate-integrating gyroscope, dynamically tuned gyroscope (DTG), single degree of freedom (DOF) integrating gyros and flex gyroscope, which

are some mechanical gyroscopes developed until today can be given as examples (Titterton & Weston, 2004).

1.1.2. Vibratory Gyroscopes

Vibratory Gyroscope begun to develop during the 1950s. It is operated by the Coriolis effect which is measured by vibrating element (Woodman, 2007). There are many geometries of vibrating micro-machining structure.

Foucault's idea that a vibrating element in a rotated system maintains its plane of vibration has been led to achieving the idea that is sensing the angular rate as well as linear velocity. As shown in Figure 3, a vibrating mass (m) in a rotating system with an angular rate (ω) about an axis orthogonal to oscillatory linear velocity (v) is exposed to Coriolis acceleration. This acceleration leads to Coriolis force (F_c) and modifies the motion of the vibrating mass (Titterton & Weston, 2004). This modification can be detected; therefore, the magnitude of the angular rate can be measured.

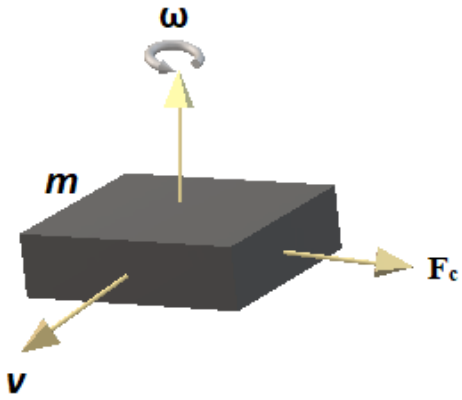

Figure 1.3 A Simple Geometry of Vibrating Mass (m)

Coriolis effect has an inertial force which acts on an object with a mass (m) moving with velocity (v) relative to a rotating reference frame at an angular velocity (ω), and

it is given in the Equation 1.1 (Titterton & Weston, 2004) (Woodman, 2007).

$$F_c = -2m(\omega \times v) \qquad 1.1$$

Examples of vibratory gyros in different geometries of the vibrating element include hemispherical resonator gyroscopes (HRG), vibrating wheel gyroscopes, tuning fork gyroscopes, vibrating disc sensor and vibrating wine glass sensor (Titterton & Weston, 2004).

The most common design of vibratory gyroscope technology has stable quartz resonator with piezoelectric driver circuit (Titterton & Weston, 2004). There are many different designs, and one of them is MEMS, which is commonly used in industry. MEMS gyroscopes have a vibrating element, and operates in the principle of Coriolis Effect (Woodman, 2007). MEMS gyroscopes which are micro-electromechanical systems are widely used in gyroscope industry because it is cheap, small (packaged in 15-25mm rectangular cases), low mass and high tolerance for shock (Groves, 2008). However, it has poor performance relative to mechanical and optical gyros due to limited fabrication technique considering that known relatively the most efficient material existing on the Earth named Silicon. Moreover, MEMS gyroscopes are used not only in expensive military devices or space applications but also in daily life such as in mobile telephones, automotive and health sector owing to cheapness and smallness.

According to its design, vibratory sensors can have a small error rate of 0.01 º/hr, but smaller sensors can produce an error rate in the region of 0.1-1 º/s. This error, called bias, is mostly influenced by environmental effects such as temperature changes and vibration as in almost all types of gyroscopes (Titterton & Weston, 2004).

1.1.3. Optical Gyroscopes

The operating principle of optical gyroscope was proposed by George Sagnac in early 20th century named Sagnac effect examined in the Heading 2.1. There are two types of optical gyroscopes: Ring Laser Gyroscope and Fiber Optic Gyroscope. Both are operated by Sagnac theory, but they have different material structure, design and measurement techniques.

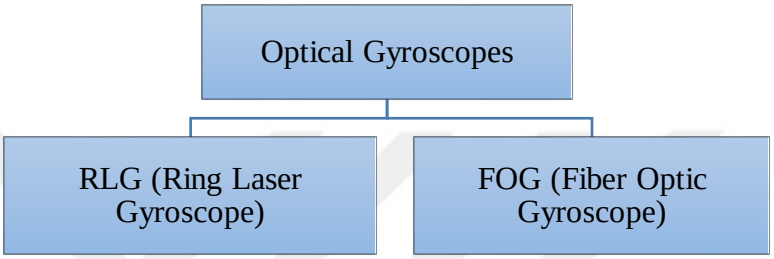

Figure 1.4 Types of Optical Gyroscopes

Optical gyroscopes have a great improvement with respect to greater reliability, smaller size and cheapness comparing with traditional mechanical gyroscopes (Passaro, Cuccovillo, Vaiani, Carlo, & Campanella, 2017). However, MEMS gyros are still smaller and cheaper, but not have higher performance than optical gyroscopes.

The Sagnac theory on paper was actually proposed in the circular geometry that looks like fiber optic coil (Lefevre, 2014). However, since fiber production was not started, the theory was adapted to RLG in which mirrors are placed next and across to each other to propagate light as shown in Figure 1.5 (Ring laser gyroscope, n.d.). Therefore, RLG technology has been improved first.

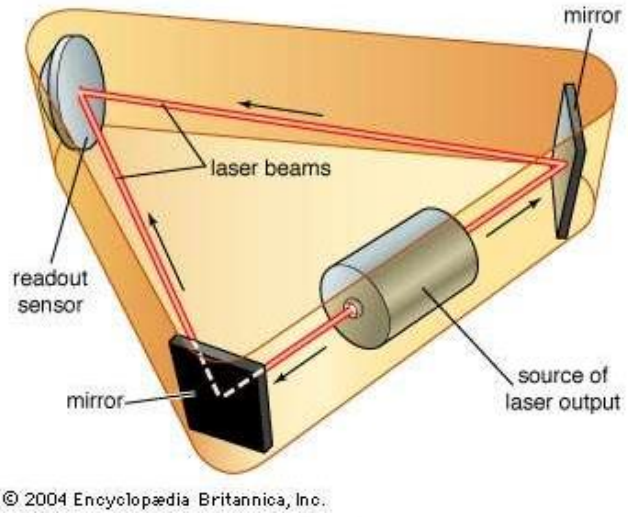

Figure 1.5 Basic Demonstration of RLG *(Ring laser gyroscope, n.d.)*

RLG was presented after the invention of helium-neon (He–Ne) laser technology in the 1960s. It was succeeded in the 1980s to take the place of classical mechanical gyroscopes about longer lifetime, wide dynamic range, reliability and good scale factor for using on strap-down navigation systems (Groves, 2008). For many years, RLG technology has dominated the optical gyroscope industry.

RLG can be designed by three or more mirrors to reflect light beams traveling opposite ways with a constant velocity. These light beams propagate in an active laser medium in the ring cavity called resonator. This medium is filled with gas that is excited by electrodes in order to create a plasma to provide the control of the stability of the capacitive discharge of the system (Pizzocaro, 2009). If there is a rotation in the system, there occurs a phase shift, which is translated directly in frequency shift. Thus, the rotation rate can be calculated from the frequency difference between two counter propagating beams. When there is not any rotation, beams which act like standing waves are in the resonance mode. In order to sustain or control laser action in the desired mode and to eliminate errors due to backscattering, the dithering mechanism is used (Passaro, Cuccovillo, Vaiani, Carlo, & Campanella, 2017). Under rotation,

occurring frequency difference is called Sagnac frequency. This measuring method is the essential difference between active RLG and FOG which measures angular rate from phase difference (Lefevre, 2014). Moreover, one of the mirrors in the cavity can move owing to a piezoelectric transducer in order to change the perimeter of the cavity. As a result, some subtle effects coming from backscattering can be prevented, and active stabilization of the optical frequency can be provided by modulation (Pizzocaro, 2009). RLG technology is used in many fields especially in inertial systems required high precision (Titterton & Weston, 2004).

The development of the fiber optic gyroscope (FOG) began in the late 1970s (Armenise, 2014) because fiber technology used in telecommunication industry started to enhance in those years. In addition, low loss optical silica fibers were first fabricated in 1970 (Fang, 2012), and the technologies of low loss couplers, fiber polarizers and integrated optics such as piezoelectric phase modulator and multifunctional integrated optical chip began to develop (Nayak, 2011). Since then, fiber optic sensor technology has been rapidly developed. Today, control grade FOGs (10 ~ 100 º/hr class), tactical grade FOGs (1.0 ~ 10 º/hr class) and navigation grade FOGs (0.1 ~ 0.01 º/hr class) have been produced in well-known firms in the world (Nayak, 2011).

When RLG and FOG technologies are compared, both have advantages and drawbacks. RLG sensitivity has reached down to 0.001º/hr, while FOG products have been still developing. Although there are many advantages of advanced RLG technology that is used in applications requiring high performance, developing FOG technology has begun to take place in gyroscope industry because of requirements of applications (Lefevre, 2014) (Passaro, Cuccovillo, Vaiani, Carlo, & Campanella, 2017). For example, whereas RLG has an active propagation medium and dithering parts that bring into the complex mechanism and large body and mass, FOG is a passive device, solid-state structure, and has no moving or oscillating parts. This leads to being robust structure preventing mechanical perturbations for FOG. Moreover, RLG mirrors should be aligned perfectly and super clean in order to increase reflected

laser intensity, instead fiber material as a waveguide does not need to be special care after fabrication of fiber material and design of the coil. Another important drawback of RLG is the plasma that influences the capacitance of the system; therefore, any variation in the plasma due to temperature, dispersion, gas mixture, density, power loss and so on, causes the change the response of the system (Pizzocaro, 2009). In terms of size, weight and cost, FOG products have advantage features because RLG products have complex mechanical and optical components (Lefevre, 2014). However, there are also many drawbacks for FOG products, which have been studied in the world. For example, noise can occur due to various reasons such as the external magnetic field, vibration, shock, optical power dependency of fiber material, the temperature dependency of fiber material (Armenise, 2014) (Fang, 2012).

As a result, it is significant to understand the characteristic features, behavior and error sources of a gyro in order to overcome problems, and enhance the technology and further calibration techniques.

FOG and RLG products should not be considered as competitive gyros, but they can be preferred for their own applications.

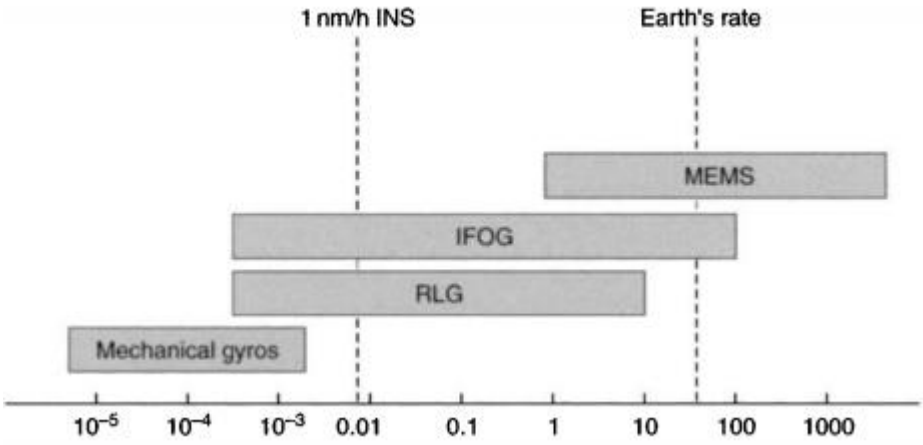

Figure 1.6 Bias Stability (°/hr) comparison of mechanical gyros, optical gyros and MEMS gyros *(Titterton & Weston, 2004)*

In Figure 1.6, the ranges of bias stability of gyroscopes in the industry are illustrated. Mechanical, optical (RLG and IFOG) and MEMS gyroscopes take place in high, medium and low performance system applications respectively (Titterton & Weston, 2004). On the other hand, especially IFOG technology is eligible to be improved by new designs, materials and methods; thus, can be reached higher performance grades with developing technology in the future (Lefevre, 2014).

Today, RLG and IFOG technologies have maintained their improvements by obtaining more know-how about their physical characteristics and sensitivities. In this thesis, FOG technology is studied in order to observe the thermal sensitivity of a FOG device.

1.2. Other Gyroscope Technologies

In the world, a number of researches for alternative class gyroscope technologies have been conducted including nuclear magnetic resonance (NMR) gyroscopes, electrostatic gyroscopes (ESG), flueric sensors, superfluid gyro (Armenise, 2014), angular accelerometers, atom interferometry techniques and rate transducers which include mercury sphere and magneto-hydrodynamic sensors (Groves, 2008). These sophisticated type of gyroscopes are called as unconventional sensors and have different instruments and novel techniques to sense rotational motion.

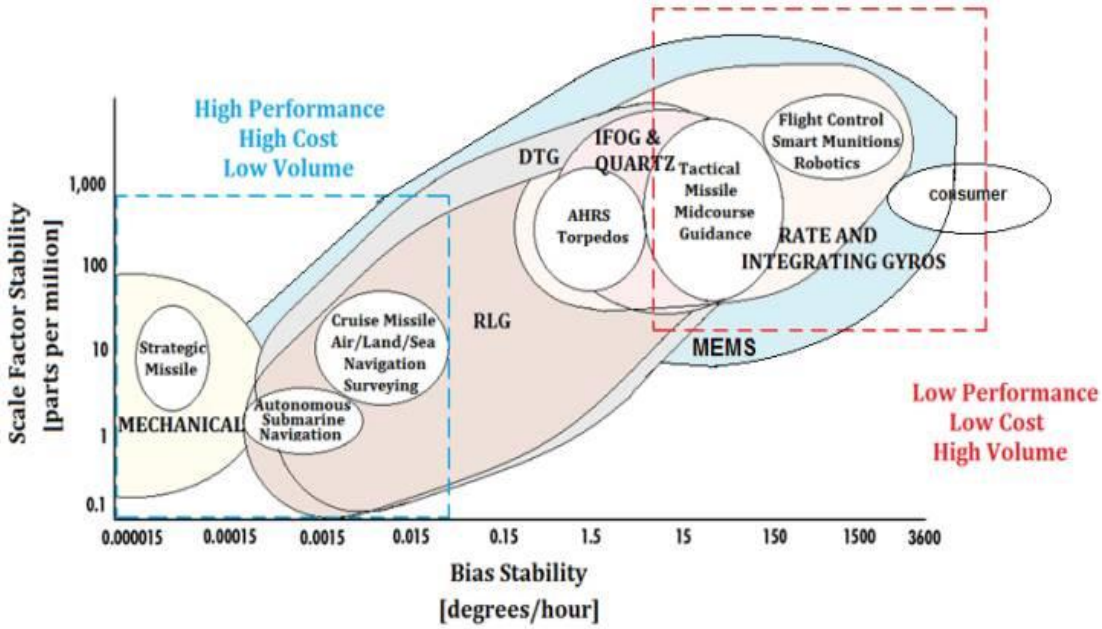

Figure 1.7 Performance Comparison of Gyroscopes by the Graph of Scale Factor Stability (ppm) vs Bias Stability (degrees/hour) *(Passaro, Cuccovillo, Vaiani, Carlo, & Campanella, 2017)*

For all classes of gyroscopes, the main issues are errors which are resulted by not only internal sources such as imperfect fabrication, design and material of the gyroscope components but also external sources such as vibration, magnetic field, humidity, acoustical effects, shock, external temperature sensitivity (Lefevre, 2014). These error sources distort the measurements of angular rate and lead to defective data. Noisy measurements influence the sensitivity of the gyroscopes.

Performance of a gyroscope depends on how sensitive rotation rate is measured and how gyroscope behavior is changing under different environmental circumstances. Therefore, there are performance parameters in order to determine the performance grade of gyroscopes. Main parameters can be specified as bias, scale factor stability, angle random walk (ARW), bias instability and quantization noise (IEEE Standard Specification Format Guide and Test Procedure for Single-Axis Interferometric Fiber

Optic Gyros, n.d.) (IEEE Standard for Sensor Performance Parameter Definitions, n.d.).

Bias means that gyro output deviation is expected to be measured zero while the system is not rotating for sensing axis (IEEE Standard for Sensor Performance Parameter Definitions, n.d.); however, there is an offset value named bias.

The scale factor is a constant value that expresses how stable or linear the relationship between the measured value and applied rate of a gyroscope. If the scale factor is not stable, that leads to scale factor errors such as scale factor nonlinearity and scale factor asymmetry (Titterton & Weston, 2004). The ratio of output error to input rate gives how good the measurements of the gyro is and denoted in ppm.

Angle random walk is always existing error caused by spontaneously emitted photons from anywhere in the IFOG (IEEE Standard Specification Format Guide and Test Procedure for Single-Axis Interferometric Fiber Optic Gyros, n.d.). ARW is calculated from Allan variance curve (Allan Variance: Noise Analysis for Gyroscopes, 2015) (Crank, 2011).

Bias instability means the random variation in bias computed over certain sample time and averaging time intervals (IEEE Standard Specification Format Guide and Test Procedure for Single-Axis Interferometric Fiber Optic Gyros, n.d.) (IEEE Standard for Sensor Performance Parameter Definitions, n.d.). Bias instability that is not a constant value can change during an operation, thus it is important to test how the stability changes.

Quantization noise is resultant of the random attribution to noise obtained from an electronic part of the gyros (IEEE Standard Specification Format Guide and Test Procedure for Single-Axis Interferometric Fiber Optic Gyros, n.d.). It is due to the random variation of the digitized output signal while sampling and quantizing a continuous signal.

In this thesis, it is focused on the operating principle of FOG and dwelled on the thermal sensitivity of optic fiber. As a result, effects of the temperature change on the bias of a FOG, which is a major error source for FOG are shown theoretically, experimentally and by simulation.

CHAPTER 2

LITERATURE REVIEW, METHODOLOGY AND APPLICATIONS

2.1. Basic Physics of Sagnac Effect

In 1913, the French physicist George Sagnac discovered that angular rate can be detected by using interferometric device (Lefevre, 2014).

According to George Sagnac, two light beams traveling in the opposite direction on the same waveguide create interference due to the phase difference that occurs when the system rotates. This interference is directly proportional to the amount of rotation of the system. Thus, how much the system rotates can be measured.

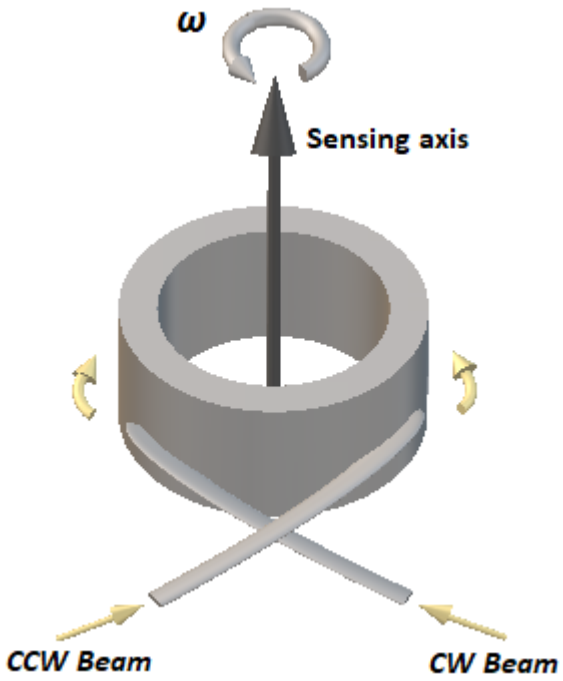

Figure 2.1 Two Light Beams Propagation in a Fiber Coil

In Figure 2.1, a drawn fiber coil is illustrated. There are two fiber cables out of the coil in order to carry two oppositely propagating light waves according to the winding scheme. Rotation rate occurs in accordance with the sensing axis passing through the center of the coil.

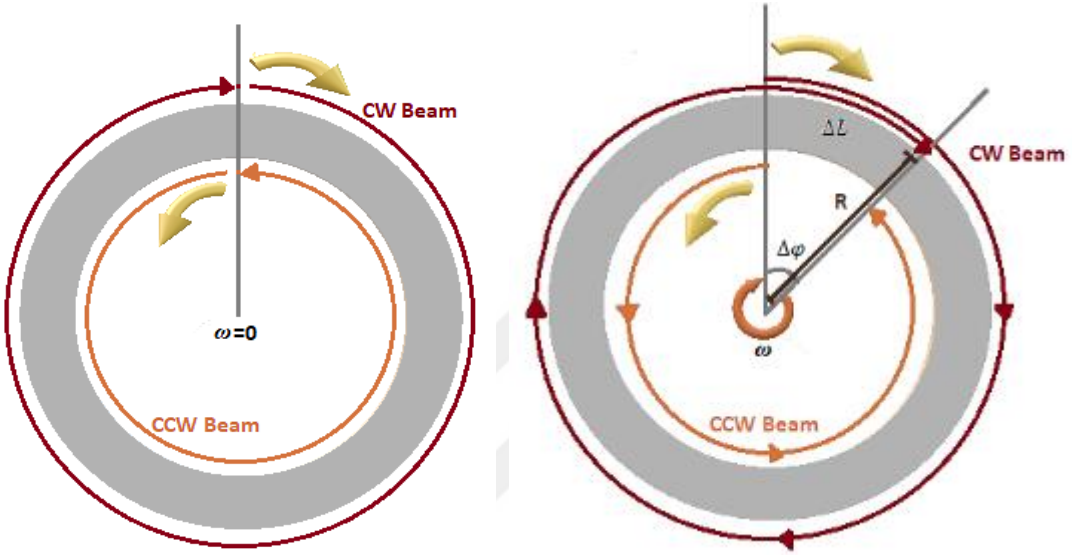

(a) (b)

Figure 2.2 Propagation directions of light waves (a) under no rotation (b) under rotation ω

In Figure 2.2, upper-sectional view of a coil is illustrated with two different situation. In the first situation (a), two light beams propagate in different directions through circular optical path such as fiber coil without any rotation in the system. After a certain transit time, two light beams arrive the end at the same time due to traveling at the same distance with the same velocity. In the second situation (b), the system rotates with an angular velocity (ω). As a result of rotation, whereas CW beam undergoes spreading through the path length, CCW beams travel less distance through the path (Heimann, Liesegang, Arndt-Staufenbiel, Schröder, & Lang, 2013). This occurrence leads to a phase shift between these counter propagating light waves.

Therefore, the angular rate can be determined by mathematically from its proportional phase shift.

Considering circular waveguide whose radius r and length L, light propagating in the direction of clockwise completes one round with speed of light in a matter "$v = c/n$" (c: speed of light in a vacuum, n: refractive index of a material) and with an angular velocity "$\omega = 2\pi v$" for a transit time "t_{cw}". CW light beam travels the whole path as $\Delta L_{CW} = R\omega t_{CW}$. Hence, its transit time is written as follows (Fang, 2012) (Shamir, 2006).

$$t_{CW} = \frac{2\pi R + \Delta L_{CW}}{v} \quad 2.1$$

$$t_{CW} = \frac{2\pi r + 2\pi r\omega t_{CW}}{v} \quad 2.2$$

$$t_{CW} = \frac{2\pi r}{v(1 - \frac{r\omega}{v})} \quad 2.3$$

In addition, CCW light beam travels the whole path as $\Delta L_{CCW} = R\omega t_{CCW}$. Hence, its transit time is written as follows.

$$t_{CCW} = \frac{2\pi R - \Delta L_{CCW}}{v} \quad 2.4$$

$$t_{CCW} = \frac{2\pi R - 2\pi r\omega t_{CCW}}{v} \quad 2.5$$

$$t_{CCW} = \frac{2\pi r}{v(1 + \frac{r\omega}{v})} \quad 2.6$$

The difference between the transit times of these two oppositely propagating beams gives rise to the phase difference between them proportional to the rotation rate in the system.

$$\Delta t = t_{CW} - t_{CCW} = \frac{2\pi r}{v}\left[\frac{1}{\left(1-\frac{r\omega}{v}\right)} - \frac{1}{\left(1+\frac{r\omega}{v}\right)}\right] = \frac{4\pi r^2\omega}{v^2}\left[\frac{1}{\left(1-\frac{r\omega}{v}\right)^2}\right] \quad 2.7$$

The tangential speed ($r\omega$) is too small ($r\omega << v$) rather than the speed of light in a matter (v) that it can be ignored (Shamir, 2006). In addition, the area (A) of the circular geometry can be added in the Equation 2.7 as $A = \pi r^2 = D^2/2$ where D is diameter.

$$\Delta t = \frac{4\pi r^2\omega}{v^2} = \frac{4A\omega}{v^2} \quad 2.8$$

Due to the time difference of two monochromatic (λ) light beams traveling counter directions, there occurs the interference which provides information about the phase difference ($\Delta\varphi$). Rotation rate (ω) of the system is proportional to this phase difference as Equation 2.9.

$$\Delta\varphi = \frac{2\pi v\Delta t}{\lambda} = \frac{8\pi A\omega}{\lambda v} = \frac{2\pi LD\omega}{\lambda v} \quad 2.9$$

As a result, the phase difference is derived as the equation below.

$$\Delta\varphi = \frac{2\pi LD}{\lambda v}\ \omega \quad 2.10$$

v is interpereted as c (speed of light for a vacuum). For an ideal case, length of material (L), diameter (D) and wavelength (λ) are constants. Thus, the phase difference is directly proportional to the angular velocity with a constant. This constant is named

scale factor (SF) which indicates how linear the measured output of the system and the applied angular velocity.

$$SF = \frac{\Delta\varphi}{\omega} = \frac{2\pi LD}{\lambda v} \qquad 2.11$$

2.2. Fiber Optic Gyroscope Technology

Fiber optic gyroscopes are categorized as interferometric fiber optic gyroscope (IFOG), resonant fiber optic gyroscope (RFOG) and Brillouin fiber optic gyroscope (BFOG) (Heimann, Liesegang, Arndt-Staufenbiel, Schröder, & Lang, 2013).

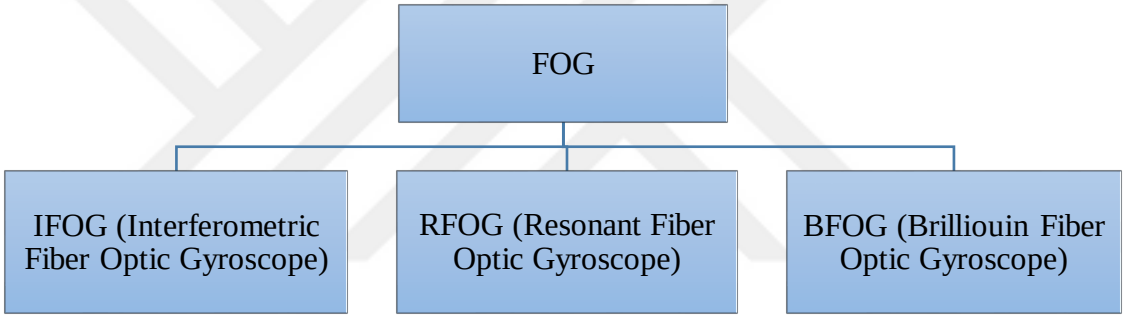

Figure 2.3 Types of Fiber Optic Gyroscopes

They all are operated by Sagnac principle. However, they differ in terms of some optical components, fiber lengths and measured parameters. Comparison list of optical components is given in Table 2.1.

Table 2.1. Comparison list of fiber optic gyroscope components

Interferometric Fiber Optic Gyroscope (IFOG)	Photodiode (1 item) Broadband Light source (1 item) Micro integrated optic chip (MIOC) 1x2 and/or 2x2 coupler Fiber Coil (with a length of a few hundred up to some thousand meters) SM and/or PM fiber
Resonant Fiber Optic Gyroscope (RFOG) (Jin, Yu, & Ma, 2013)	Photodiode (2 items) Narrowband Light source (2 items) Acoustic-optic frequency shifter (AOFS) or Acousto-optic modulator (AOM) 1x2 or 2x2 coupler Fiber ring resonator (can be one loop with radius 12cm) Air core fiber
Brilliouin Fiber Optic Gyroscope (BFOG)	(Design has been still in developing process (Nayak, 2011) (Ponikvar & Ezekiel, 1981)

The operating theory of IFOG, RFOG and BFOG is the same, which is the Sagnac effect. On the contrary, the main difference between them is their measurement techniques. In IFOG, the rotation rate is measured by its relationship with the phase difference between two oppositely propagating light beams. In RFOG and BFOG, angular rate is related with frequency shift between these two beams. Required optical components differ according to the measurement techniques. For example, MIOC is

used for phase modulation in IFOG, while AOM is used as frequency shifter for modulation in RFOG.

IFOG has long PM or SM fiber length from 100 m to 3000 m in order to be able to sense a small phase shift. RFOG design is based on increasing the effect with recirculation in the resonant cavity of a ring laser instead of using the numerous loops as in IFOG. RFOG fiber material differs from IFOG in order to reduce the error in the measurement caused by ambient temperature changes, external magnetic field and applied power (Benser, Sanders, Smickilas, Wu, & Strandjord, 2015). Besides, it is aimed to be short fiber length for lower mass, volume and sensing coil cost in RFOG (Jin, Yu, & Ma, 2013).

Optical design configuration of BFOG is considered to be simple. It is aimed to be a wider dynamic range. High power light source is preferred to pump the laser to ring resonator, and stimulated Brillouin scattering is induced to the resonator. The beat frequency is created by different path lengths that two beams travel around. The gain phenomenon of Brillouin fiber ring laser into the cavity is studied in order to obtain frequency change of under rotation (Ponikvar & Ezekiel, 1981).

Many industrial and tactical grade Interferometric fiber optic gyroscope products are produced. In industry, navigation grade IFOG sensors are also available (Korkishko, et al., 2017), and researchers in the world are still studying for better performance grades.

RFOG is newly developing technology in today's world. There has not been commercial product yet, but some leader firms in the field of gyroscope technology are known to work on it (Lefevre, 2014). Moreover, it is predicted that BFOG will be the future technology, so there are few researches and articles for now. It is needed to fully understand the working principle of error mechanism of the technology in order to enhance the new technology.

2.3. An Overview of Interferometric Fiber Optic Gyroscope Technology

Evolution of IFOG technology requires deep learning and researches about its operational conditions and physical behaviors. In Figure 2.4, the optical configuration of IFOG is illustrated. This illustration is the most basic (minimum) reciprocal geometry for an IFOG device.

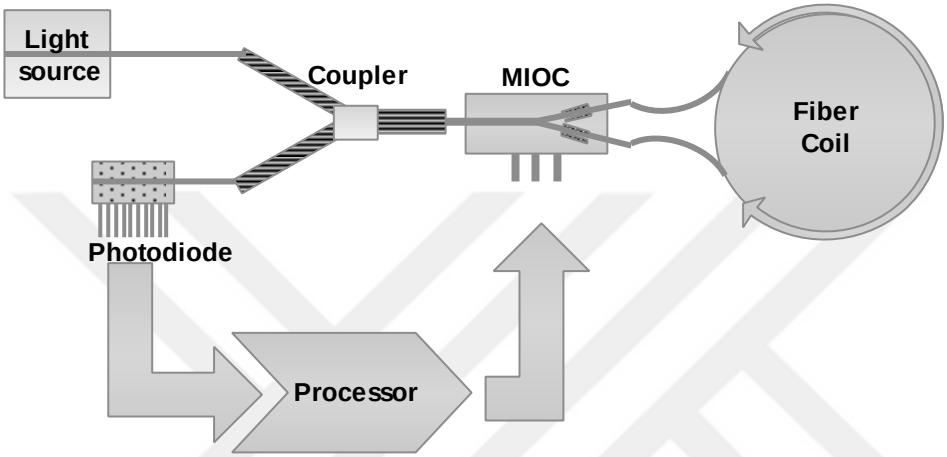

Figure 2.4 The Most Basic Reciprocal Configuration of IFOG

Reciprocity is the key important occurrence for IFOG. It tells about how much symmetry there are in the system. In a reciprocal system, the counter propagating light beams must travel exactly the same path (Lefevre, 2014). In other words, both beams in the directions of clockwise and counter clock-wise, reflect and transmit when passing through the couplers or called splitters. During operation, these two optical signals should have the same amount of reflections and transmissions; therefore, they should arrive the photodetector in phase when the system is at rest. If the system is not reciprocal, that means there is power imbalance between two beams and a phase shift existing in the detector even if the gyro is at rest (Armenise, 2014). Reciprocity problem can be solved by adapting a reciprocal configuration to the optical system.

IFOG optical architecture consists of a light source, couplers, MIOC, fiber coil and photodetector. Before using polarization maintaining (PM) fibers, IFOG included polarizers and depolarizer. There can be distinct designs of architecture in FOG industry.

In IFOG, a broadband light source is used such as superluminescence diode (SLD) or Er^{+3} doped fiber source (EDFS) because light sources with a small coherence length is required in order to eliminate errors caused by optical nonlinearities (Heimann, Liesegang, Arndt-Staufenbiel, Schröder, & Lang, 2013).

Couplers are used for splitting and recombination of light powers traveling in the system. Therefore, two light beams can be divided to the different paths, or lights coming from different paths can be combined in one path. There are various kind of couplers in industry such as X-coupler, Y-coupler, star coupler and so on (Lefevre, 2014). According to design, desired type of coupler can be used as long as the reciprocal configuration is provided.

MIOC is an opto-electronic(optoelectronic) component that is composed of Lithium niobate ($LiNbO_3$)-based Y junction waveguide structure. MIOC is the key component that influence the FOG accuracy. It is a phase modulator, which can create the response to the closed loop feedback signal of the system (Yi & Wen, 2006). It also performs as a Y-coupler and a polarizer. Power of light passing through MIOC is divided into half of the initial intensity and directed to two different paths through the fiber coil (Lefevre, 2014).

The sensing part of IFOG is the fiber coil. Light beams can symmetrically propagate with respect to the center of the coil; hence, the angular rate is calculated according to this reference rotating frame. The length of fiber coil can be a few hundred up to some thousand meters in order to increase the resolution in the measurement.

A photodetector, which is the end of the optical path, senses the optical power and transduce it to electrical power. With the developing opto-electronic technology, PIN-

FET photodiodes are preferred to obtain highly efficient power because PIN-FET diodes have a good quantum efficiency (Lefevre, 2014).

2.4. Optical Difficulties of Fiber Optic Gyroscope

It is essential to understand the principle of operation of FOG in order to integrate into various applications in land, sea, air and space. In addition, improving the system to higher performance grades is required in fact that its error sources and limitations should be well investigated.

Fiber optic gyroscopes have many optical error sources that cause noisy data at the output of the system that contributes to bias, bias instability, scale factor accuracy and ARW of the FOG. There are also many solution proposals in literature for these problems in order to minimize the noisy effects. Although there is not any solution that completely solves the problems, there are significant improvements owing to finding out new methods as well as researching the theory and characteristics of error sources behavior.

In FOG, light propagates through its waveguide of fiber material and some integrated optical components. Because of the physical property of the fiber material, optical components and light itself, parasitic effects such as backscattering, back reflections, nonreciprocal polarization coupling and birefringence, magneto-optic Faraday effect, the nonlinear Kerr effect and Shupe effect are encountered ((Lefevre, 2014) (Shupe, 1980)). Furthermore, there are noises due to the electronic part of FOG that cause offset in the measurement. They also need to be analyzed, but they are not investigated in this thesis.

The problem of backscattering (especially Rayleigh backscattering (Fang, 2012)) and back reflection are resulted by impurities in the waveguide. These impurities can be caused by fabrication of fiber, splicing one fiber to another and pigtailing fiber to

electronic component. They lead to loss of light power, attenuation and parasitic interferences. They can be eliminated by using broadband light sources operated by amplified spontaneous emission theory (Hecht, 2017) due to its low temporal coherence (Lefevre, 2014). Besides, careful design of components and packaging help to reduce the spurious phase differences (Fang, 2012).

Moreover, the problem resulted by different polarization modes and birefringence occur in single mode fiber because of the shape of the core in fiber. Fiber core, which is the waveguide, cannot be in a perfect circular shape, so electromagnetic wave travels undesired optical paths randomly in the core. This kind of single mode optical fiber has short birefringent characteristics (Matsumoto, 2006). If input light is in a particular polarization state, and also output light is in the same polarization state, there is not any difference in the reciprocal configuration. However, input optical pulse generally divided into two parts with traveling distinct path due to the elliptical core, so each reaches the output at different times. Therefore, reciprocity of the optical system is broken down, and output waveforms and phase difference are distorted (Matsumoto, 2006). So, the undesired phase difference is read at the output. This problem can be overcome by using polarization maintaining fiber and broadband sources. Furthermore, the ellipticity of the fiber core can be influenced by the change in the ambient condition such as temperature.

Fiber optic gyroscopes are also sensitive to environmental magnetic fields. Magneto-optic Faraday effect influences the polarization state of the electromagnetic wave. In an ideal condition, both CW and CCW waves are affected by the same conditions, so that Faraday effect could be canceled out. However, there exists cross-coupling between two polarization modes, and the effects accumulates over the long fiber coil. Therefore, it is impossible to obtain symmetric distribution with respect to the center of the fiber coil. Faraday rotation can also occur due to the design of the fiber cables. Especially, the fiber twisting causes polarization plane rotation (Fang, 2012). This error can be minimized by using polarization maintaining fibers.

The nonlinear Kerr effect is related third order electric polarization (Fang, 2012). Kerr effect results from optical intensity, which influences the refractive index of the waveguide. When light beam splits from a coupler as CW and CCW beams, optical intensities of them are equal with each other in the ideal world. However, in reality, 50:50 couplers are not perfect, so that it brings into power imbalance between CW and CCW beams. Therefore, reciprocity rule cannot be preserved, and nonreciprocal index difference occurs. Thus, randomly varying optical power leads to the error of the rotation signal (Lefevre, 2014). Unfortunately, this effect accumulates in long fiber coils. But, this effect is assumed small to neglect, if the low coherent light source is used. Because nonlinear index grating created by the interference of CW and CCW wave yields a standing wave, the short coherence length is the opposite of this standing wave with an equal distance. Hence, the formation of the nonlinear index grating can be canceled out, and Kerr effect reduces (Armenise, 2014).

Shupe effect is a critical and challenging nonreciprocal problem in FOG technology. It is the time-varying refractive index perturbations across the fiber coil due to temporally thermal changes (Shupe, 1980). For an IFOG, thermal disturbance of the fiber material is considered the largest problem when other error factors can be optimized (Fang, 2012). External temperature fluctuation influences the strain of the refractive index of the fiber, which changes optical elasticity of fiber material. Besides, temperature gradients lead to the source wavelength change and decrease of sensitivity of the sensor; therefore, bias changes with changing thermal conditions (Titterton & Weston, 2004).

In the book of Advances in Gyroscope Technologies, authors indicated that “Silica refractive index depends also on temperature (a temperature change of 1K induces a refractive index change of about 10-5), which means that time-varying temperature gradients along the fiber coil can induce inaccuracies in the sensor response, according to Shupe effect.”.

There have been many coil winding (Lad, 1999) model being developed to minimize this error such as dipolar (Lefevre, 2014), random-wound coil (Dyott, 1996), cross, crossover-free (Li, Ling, Xu, & Wei, 2015), double cylinder winding (Ling, ve diğerleri, 2016) quadrupole (Li, Ling, He, Xu, & Du, 2016) and octupole (United States of America Patent No. US20090141284A1, 2007) winding methods which affect the performance of gyroscope directly (United States of America Patent No. US5917983A, 1996). Moreover, the Shupe effect requires a careful mechanical design of the potting of the coil (Bi, Sun, Wu, & Zhao, 2011). In this thesis, the thermal dependency of an IFOG is observed by tests with different temperature profiles, investigated mathematically, and heat transfer of fiber coil is simulated.

CHAPTER 3

THEORETICAL APPROACH TO TEMPERATURE DEPENDENCY OF FIBER OPTIC COIL

With the invention of fiber optic cable in the 1920s (Fang, 2012), control of the propagation of light without any limitation is a great success that leads to developing many applications such as telecommunication, medical, automotive, sensor technology and so on.

Fiber optic cables are designed as a cylindrical dielectric waveguide, which is usually made of fused silica glass because silica glass (Silicon dioxide - SiO_2 made of the most common elements on earth, silicon (Si) and oxygen (O2)) is a low-loss material and has high chemical purity (Saleh & Teich, 2009).

A commercial fiber cable can have a multiple numbers of layers named core, cladding, coating and jacket surrounded by each other as shown in Figure 3.1 (Fang, 2012).

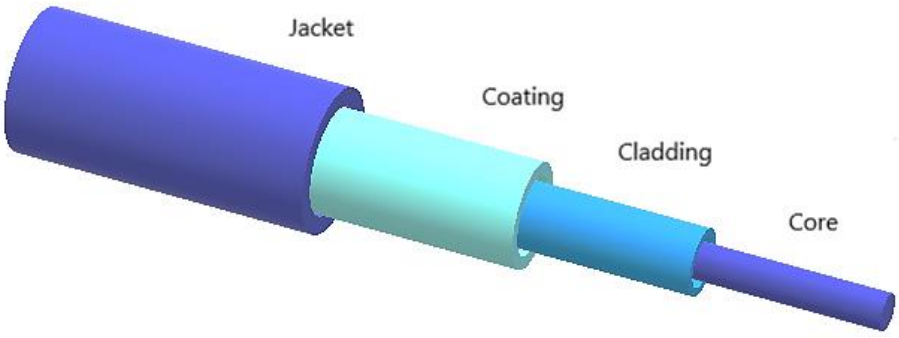

Figure 3.1 A Commercial Fiber Optic Cable

In fiber optic gyroscope technology, core and cladding are main layers to work with. Fiber optic guides light waves by the principle of total internal reflection (TIR) (Hecht,

2017). Light beams propagate through the core by reflecting from the boundary of cladding without refracting into the cladding, since core has higher refractive index than cladding ($n_{core}>n_{cladding}$), so that the boundary allows total internal reflection of beams (Saleh & Teich, 2009).

The temperature dependency of the refractive index of optical fiber material is a crucial issue as reported by the reference (Yong, Qi, & Jin, 2014). Because fiber optic material is Silica made of Si-O bonds, the theoretical explanations of the fact that how these bonds are influenced by temperature changes are based on the structural details of the solid fused silica. Therefore, according to (Yong, Qi, & Jin, 2014), the equation of dependency is as follows.

$$n_{SiO2} \approx \sqrt{\frac{3\varepsilon_0 a + 2Nq^2}{3\varepsilon_0 a - 2Nq^2}} + \frac{9Nqbk_b}{2aE_c\sqrt{(3\varepsilon_0 a + 2Nq^2)(3\varepsilon_0 a - Nq^2)}}T \qquad 3.1$$

where N indicates the average number density of the Si–O bonds along the direction of the local electric field E_c and N = 4.883×10^{28} m^{-3}. The local electric field is E_c =1×10^{11} $V\cdot m^{-1}$, vacuum permittivity ε_0 =8.854×10^{-12} $F\cdot m^{-1}$, polarizability is a =1.779×10^{2} $J\cdot m^{-2}$, the volume energy density is b=1.265×10^{12} $J\cdot m^{-3}$, electric charge is q=1.647×10^{-19} C, and Boltzman constant is k_b=1.381×10^{-23} $J\cdot K^{-1}$. The variables n and T are refractive index and temperature, respectively.

As a result, refractive index of silica fiber is directly proportional to temperature (Yong, Qi, & Jin, 2014).

$$n_{SiO2} \approx 1.47269 + 7.09780\times 10^{-6}T \qquad 3.2$$

Temperature dependency of Silica material is proposed by various parameters as indicated above. Moreover, considering fiber optic gyroscope, Silica expansion coefficient (α_{SiO2}) along the length of the fiber (L) and thermal dependence of Silica

refractive index ($\frac{dn_{SiO_2}}{dT}$) operating at a certain wavelength are other important parameters. Thermal dependence of Silica index for 1550 nm is given as $8.4x10^{-6}/°C$ (Lefevre, 2014).

If refractive index of a waveguide varies with changing temperature, light beams will propagate different paths in a waveguide. That means CW and CCW beams begin traveling distinct modes, and both interfere with a time delay at the output of the system. Because of thermal distortions, the birefringence of the fiber also changes (Titterton & Weston, 2004). This is the Shupe effect that causes undesirable phase shifts due to thermally induced non-reciprocity, which contributes to bias, bias stability and ARW of fiber optic gyroscope (Lefevre, 2014). Besides, thermal changes alter the length and the thickness of the coil resulting in changes in the scale-factor of the gyroscope as shown in Equation 2.11 (Titterton & Weston, 2004).

The effects of time-varying thermal gradients arises in the fiber coil where is expected to generate the phase shift related to rotation rate. However, the thermal gradients accumulate the phase error over phase shift due to rotation along the length of the fiber coil (Lofts, 1995).

Light beam with wavelength λ results in a phase shift φ for an infinitesimal length l through the length of a fiber coil L.

$$\frac{\varphi}{l} = \frac{2\pi}{L} \tag{3.3}$$

As linear velocity $\vec{v} = \vec{r}\ x\ \vec{\omega}$ has the components of the radius of the coil r, angular velocity ω, the length of the fiber coil L can be written with linear velocity v and period that a light beam completes a tour through the coil in a time t as $L = v * t$. Besides, the equations of $v = \frac{c}{n}$ with speed of light c and cladding refractive index n (Shupe, 1980) and $t = \frac{\lambda}{c}$ are added in Equation 3.4.

$$\frac{\varphi}{l} = \frac{2\pi}{v * t} = \frac{2\pi}{\frac{c}{n}\frac{\lambda}{c}} \qquad 3.4$$

After rearranging the Equation 3.4, the phase shift can be written as follows.

$$\varphi = \frac{2\pi n}{\lambda} l \qquad 3.5$$

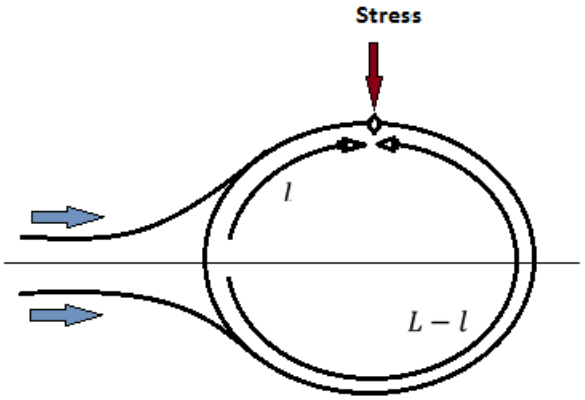

Figure 3.2 Thermal perturbation at the location of l in the fiber coil

A phase shift is generated at the infinitesimal fiber segment (δl) in a curvilinear coordinates which can be expressed as following (Lefevre, 2014).

$$\delta\varphi = \frac{2\pi n}{\lambda} \delta l \qquad 3.5$$

The phase error is proportional to the temporal derivative of temperature during both getting warming and cooling. There occurs a variation in this phase shift with thermal change dT. Therefore, derivative of Equation 3.5 gives the variation of refractive index with respect to temperature change as in the Equation 3.6. Temperature derivative of the refractive index of fiber material along the fiber length L is expressed

as $\frac{dn}{dT} = \frac{dn_c}{dT} + n_c \frac{dL}{LdT}$ where n_c is refractive index of fiber core whose material is SiO_2. Moreover, $\frac{dL}{LdT} = \alpha_{SiO2}$ is the thermal expansion coefficient of fiber material Silica (Lefevre, 2014) (Shupe, 1980).

$$d(\delta\varphi) = \frac{2\pi}{\lambda}\left(\frac{dn_c}{dT} + n_c\alpha_{SiO2}\right).\mathrm{dT}.\delta l \qquad 3.6$$

where $\frac{dn}{dT}$ is temperature dependence of the refractive index of Silica that is 8.4x10^{-6} /°C, and α_{SiO2} is thermal expansion coefficient that is 0.5x10^{-6} /°C, and thus $\frac{dn}{dT} + n\alpha_{SiO2} \cong 9x10^{-6}/°\mathrm{C}$ (Lefevre, 2014). These approximations are valid for single mode fiber (Shupe, 1980).

For an asymmetric perturbation at the distance l as shown in Figure 3.2, counter rotating beams become traverse beams due to the stress of temperature, so that there occurs a time delay between them as follows.

$$\Delta t(l) = \frac{(L-l)}{\frac{c}{n_c}} - \frac{l}{\frac{c}{n_c}} = \frac{L-2l}{\frac{c}{n_c}} \qquad 3.7$$

Since the temperature varies with time and position in fiber $\left(\frac{\mathrm{dT}(l)}{dt}\right)$, the phase error over a time interval at the point l ($\Delta t(l)$) is written as follows by referring the equation 3.7 (Shupe, 1980).

$$\delta\varphi(l) = \frac{2\pi}{\lambda}\left(\frac{dn_c}{dT} + n_c\alpha_{SiO2}\right).\frac{\mathrm{dT}(l)}{dt}.\frac{L-2l}{\frac{c}{n_c}}.\delta l \qquad 3.8$$

$\frac{\mathrm{dT}(l)}{dt}$ is noted as Tdot ($\dot{T}$) (Lefevre, 2014). In Equation 3.8, the elementary phase error is found. The two oppositely travelling beams are exposed to that perturbation at the

point l for one and $L-l$ for the other. Therefore, the total phase error $\delta\varphi_e(l)$ is generated as $\delta\varphi_e(l) = \delta\varphi(l) + \delta\varphi(L-l)$, and the accumulated phase error can be written by integration of the Equation 3.8 as follows.

$$\varphi_e(l) = \frac{2\pi n_c}{\lambda c}\left(\frac{dn_c}{dT} + n_c\alpha_{SiO2}\right)\int_0^L (L-2l)\left[\dot{T}(l) - \dot{T}(L-l)\right]dl \qquad 3.9$$

This mathematical demonstration is called the pure Shupe effect (Lefevre, 2014). If the fiber coil is assumed to be wound symmetrically, then two counter propagating beams affect the similar disturbance at the same time as shown in Figure 3.3 (Lefevre, 2014) (Shupe, 1980).

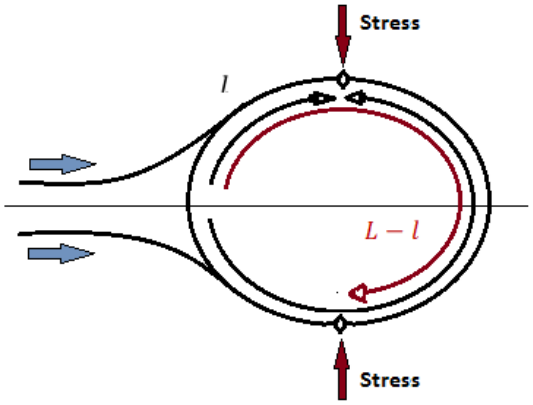

Figure 3.3 Perturbations with symmetric winding coil

If the Equation 3.9 is calculated considering perfect symmetric windings, the pure Shupe effect is canceled out as $\dot{T}(l) - \dot{T}(L-l) \approx 0$. Moreover, if these winding techniques are symmetric around $l = L/2$, the Equation 3.9 vanishes (Shupe, 1980). The following equation can be written by rearranging the Equation 2.10 by using the Equation 3.9. Note that the symbols ω is used as rotation rate and Ω_E is used as rotation rate error.

$$\Omega_{E1} = \frac{n_c}{DL}\left(\frac{dn_c}{dT} + n_c\alpha_{SiO2}\right)\int_0^L \left[\dot{T}(l) - \dot{T}(L-l)\right](L-2l)dl \qquad 3.10$$

As a result of Equation 3.10, Shupe effect does not depend on Tdot (Ṫ), but it depends on delta Tdot. In pure Shupe effect equation, it is assumed that the thermal dependency of the incremental phase $\left(\frac{dn_c}{dT} + n_c\alpha_{SiO2}\right)$ is same for the two elementary segments of the symmetric points as shown in Figure 3.3. It is obvious to see that the integration of the weighting factor $(L-2l)$ shows in the fact that every two points in the fiber is equidistant to midpoint of fiber coil.

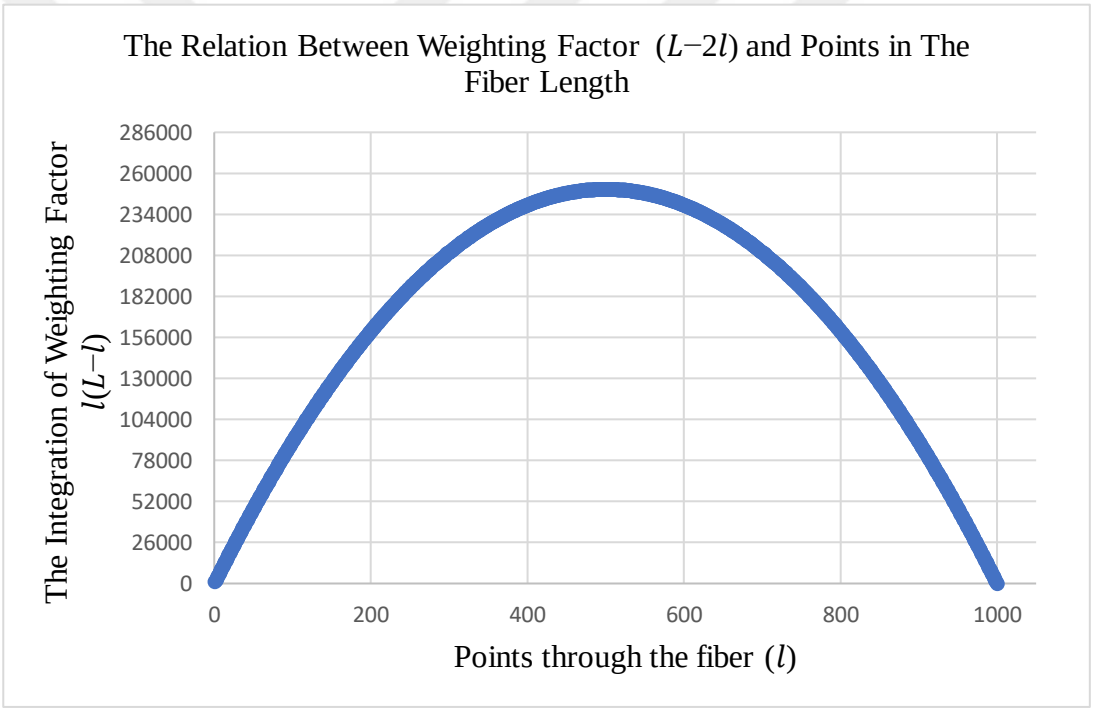

Figure 3.4 The point symmetry for the fiber length of 1000 m with respect to the midpoint in 500m

In Figure 3.4, it can be checked the symmetric points have equal distances to the given midpoint at 500 m for the total fiber length of 1000 m. Therefore, the weighting factor is true element in integration for symmetrical wound coil.

However, the fiber experiences the non-uniform thermal stresses (Lefevre, 2014). Assuming $\alpha_T = \frac{dn_c}{dT} + n_c\alpha_{SiO2}$, there should be two different coefficients of thermal dependence as $\alpha_T(l)$ and $\alpha_T(L-l)$. Hence, Ω_{E1} evolves Ω_{E1T}as follows.

$$\Omega_{E1T} = \frac{n_c}{DL}\int_0^L \left[[\alpha_T(l).\dot{T}(l)] - [\alpha_T(L-l).\dot{T}(L-l)]\right](L-2l)dl \qquad 3.11$$

Equation 3.11 can be written with a mathematical trick as follows (Lefevre, 2014).

$$\Omega_{E1T} = \frac{n_c}{DL}\int_0^L \left\{\left[\left(\frac{\alpha_T(l)+\alpha_T(L-l)}{2}\right)\left(\dot{T}(l)-\dot{T}(L-l)\right)\right] + \left[\left(\alpha_T(l)-\alpha_T(L-l)\right)\left(\frac{\dot{T}(l)+\dot{T}(L-l)}{2}\right)\right]\right\}(L-2l)dl \qquad 3.12$$

In equation 3.12, the first bracket refers to pure Shupe effect and the second bracket refers to the Tdot effect. This equation can be rearranged as the mean of thermal expansion coefficient $<\alpha_T>=\frac{\alpha_T(l)+\alpha_T(L-l)}{2}$, change in time dependent temperature $\Delta\dot{T} = \dot{T}(l) - \dot{T}(L-l)$, change in thermal expansion coefficient $\Delta\alpha_T = \alpha_T(l)-\alpha_T(L-l)$ and mean of time dependent temperature $<\dot{T}>=\frac{\dot{T}(l)+\dot{T}(L-l)}{2}$. As a result, the final form is as follows (Lefevre, 2014).

$$\Omega_{E1T} = \frac{n_c}{DL}\int_0^L \left\{\left[(<\alpha_T>)(\Delta\dot{T})\right] + \left[(\Delta\alpha_T)(<\dot{T}>)\right]\right\}(L-2l)dl \qquad (27)$$

Therefore, the main effect results from Tdot that refers to the effect of temperature-dependent stresses because non-uniform temperature-dependent stresses rise quickly, but its decay is much slower. That is why Tdot effect can be modeled rather than Shupe effect because its effect can be more observable (Lefevre, 2014).

The Tdot effect is defined in Herve Lefevre's book named "Fiber Optic Gyroscope". In addition, this Tdot effect is studied as elasto-optic effect in the literature (Mohr & Schadt, 2008) (Zhang, Gao, Wang, & Gao, 2014) . Considering fiber optic material that is Silica (SiO_2), it is important to examine elasto-optic effect of the fiber coil in order to understand temperature-dependent stresses better. The elasto-optic effect in Sagnac interferometry is related to the change in mechanical stress of fiber material (Mohr & Schadt, 2008) as illustrated in Tdot effect (Lefevre, 2014). For a fiber coil, different strains in distinct places due to temperature change lead to non-reciprocity between two counter propagating beams because strains and stress due to photo-elasticity (Mueller, 1937) are proportional to birefringence. Hence, thermally disturbed fiber material gives rise to rate error (Zhang, Gao, Wang, & Gao, 2014).

In addition to in the fact that fiber material is affected under temperature stress, parameters of refractive index of Silica (n) and length (l) strain vary due to elasto-optic effect assuming λ is constant. From the equation 18, the variable phase shift can be written as follows.

$$\Delta\varphi = \frac{2\pi}{\lambda}(n\Delta l + l\Delta n) \qquad 3.13$$

In Figure 3.5, the direction of the thermal stress is shown in two parts as on a fiber coil (a) and a cross-section of a single fiber (b). The stress of upward direction is referred to as axial strain P_a and the radial direction as P_r.

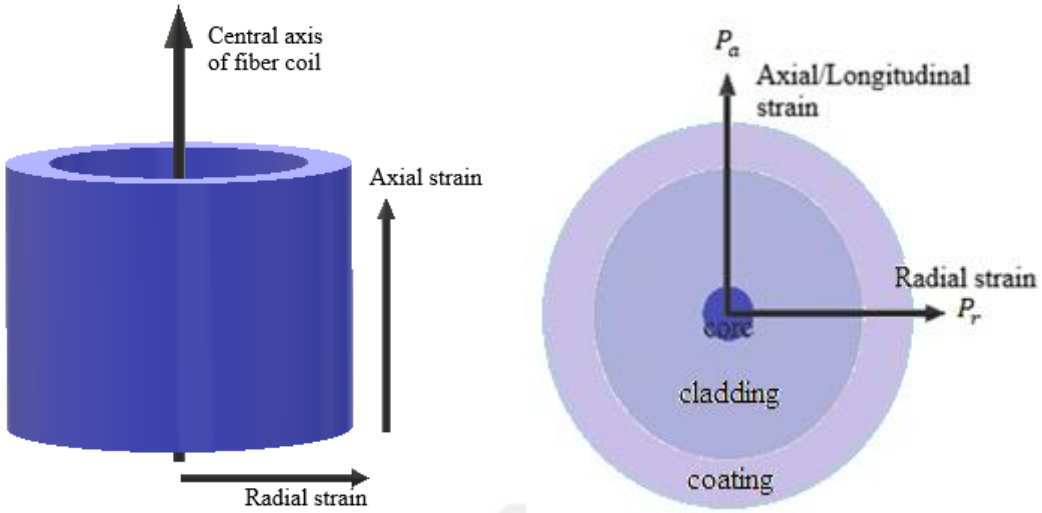

(a) (b)

Figure 3.5 Strain directions due to change of temperature (a) for a fiber coil, (b) for a cross-section of a fiber

The change in fiber refractive index Δn and the change in the length Δl are expressed as follows (Zhang, Gao, Wang, & Gao, 2014).

$$\Delta n = \frac{n^3}{2E_{core}}\{P_a[a_{11}\mu - a_{12}(1-\mu)] - P_r(a_{11} - 2a_{12}\mu)\} \qquad 3.14$$

where P_a is axial stress, P_r is radial stress, a_{11} and a_{12} are photo-elastic coefficients (called also stress-optic constants (Mueller, 1937)), μ is Poisson's coefficient and E_{core} is Young's modulus of fiber core.

$$\Delta l = \frac{-(P_a + P_r)\mu}{E_{core}} l \qquad 3.15$$

When the Equations 3.14 and 3.15 are substituted into the Equation 3.16, the phase difference is found as the following equation.

$$\Delta\varphi = \frac{2\pi}{\lambda}\left(n\left[\frac{-(P_a+P_r)\mu}{E_{core}}l\right] + l\left[\frac{n^3}{2E_{core}}\{P_a[a_{11}\mu - a_{12}(1-\mu)] - P_r(a\_11 - 2a_{12}\mu)\}\right]\right) \quad 3.16$$

Fiber coating expansion can also be taken into account because its thermal stress leads to the nonreciprocal phase difference. Thus, the parameters of $E_{coating}$ (Young's modulus of fiber coating) and α_c (thermal expansion coefficient of fiber coating) are also helpful for calculation of rate error. If the fiber coil is wound with symmetric winding techniques such as quadrupole winding, it is assumed that axial and radial stresses are equal to each other. As a result, $P_a = P_r = P = -E_{coating}.\alpha_c.\Delta T(t)$ (Zhang, Gao, Wang, & Gao, 2014) is substituted into the Equation 3.16 and rearranged as follows.

$$\Delta\varphi = \frac{2\pi}{\lambda}\left[E_{coating}.\alpha_c.\Delta T(t)\right]\left[\left(\frac{2\mu n}{E_{core}}\right)l + l\left(\frac{n^3}{2E_{core}}\right)(a_{11} - a_{11}\mu + a_{12} - 3a_{12}\mu)\right] \quad 3.17$$

Therefore, according to Equation 2.10, when the Sagnac effect phase shift is taken into account and rate error due to thermal variations, Equation 3.18 can be written as follows (Zhang, Gao, Wang, & Gao, 2014) .

$$\Omega_{E2} = \frac{c}{DL}\int_0^L \left[\frac{2n\mu}{E_{core}} + \frac{n^3}{2E_{core}}(a_{11} - \mu a_{11} + a_{12} - 3\mu a_{12})\right].\left[E_{coating}.\alpha_c.\Delta T(t)\right]dl \quad 3.18$$

where Ω_{E2} is rotation error that includes rate error with thermal stress in the first bracket and thermal stress induced by fiber coating expansion in the second bracket.

$E_{coating}$ is Young's modulus of fiber coating. D is the average diameter of fiber coil. L is the length of fiber coil, $\alpha_c$is thermal expansion coefficient of fiber coating, and $\Delta T(t)$ is temperature variation with respect to time (Zhang, Gao, Wang, & Gao, 2014).

As a result, in order to find the total rate error Ω_E, the Equation 3.10 and 3.18 should be summed up as follows.

$$\Omega_E = \Omega_{E1} + \Omega_{E2} \qquad 3.19$$

It is significant to study on principle of heat diffusion in order to understand how heat transfers through the fiber coil. Diffusion is a physical process that molecules in a matter randomly flow with their kinetic energy from a region of the system to another region. Considering optic fibers exposed to temperature variation, heat conduction theory in a steady state condition is fit to define the occurrence (Lefevre, 2014). Heat diffusion mechanism by conduction has also random molecular motion, which based on the theory that when there is a temperature difference in a material, heat power flows with the rate of the heat transfer that is proportional to the concentration gradient (Crank, 2011).

$$R = -D_i \frac{\partial C}{\partial x} \qquad 3.20$$

where R is the rate of heat transfer, C is the concentration of diffusing material, x the space coordinate which is measured normal to the area and D_i is the diffusion coefficient or diffusivity of the material (Crank, 2011). In Equation 3.20, the negative sign means that diffusion occurs in the opposite direction of the incremental concentration. In other words, heat transfers in the direction of decreasing temperature (Xiong, 2010). It is assumed to work with an isotropic medium, which the flow of thermal condition for all directions of a material has the same structure and diffusion property.

There are many solutions in order to obtain the diffusion equation for various boundary conditions. For the steady state condition, the general differential law by Fourier's law between heat flow vector q_h and the gradient vector of the temperature (Lefevre, 2014).

$$q_h = -K.\Delta T \tag{3.21}$$

where q_h is heat flow vector, K is thermal conductivity which is the ability to transfer heat in unit of W/(K.m) and ΔT is a temperature difference in the unit of Kelvin (Lefevre, 2014). For an assumption of homogeneous medium with no internal temperature and constant D_i, the heat transfer equation is as follows (Crank, 2011).

$$\Delta^2 T - \frac{1}{D_i}\frac{\partial T}{\partial t} = 0 \tag{3.22}$$

Where D_i is related to the following equation (Lefevre, 2014).

$$D_i = \frac{K}{\rho.c} \tag{3.23}$$

where ρ is the density of the material. The Equation 3.22 is related to the continuity equation that describes the transport of some quantity (Hecht, 2017). Typical diffusivity value of Silica is given as 1.0 mm^2/s (Lefevre, 2014).

CHAPTER 4

EXPERIMENTAL APPROACH TO TEMPERATURE DEPENDENCY OF FIBER OPTIC COIL

In the experiment, it is focused to observe how the rate measurements change with regard to the change in ambient temperature although the commercial gyroscopes under tests are well calibrated by its firm. The results of rate errors are obtained from residual errors. If the gyros were not calibrated, it would be seen a more obvious trend from the results of rate errors ((Zhang, Gao, Wang, & Gao, 2014) (Lofts, 1995) (Mohr & Schadt, 2008)). Moreover, residual errors can also give an idea of how sensitive the fiber optic gyros are to ambient temperature change.

In the experiment, two fiber optic gyros with different performances from KVH Inc, Firm named DSP1750 and DSP1500 are exposed to temperature profiles.

(a) (b)

Figure 4.1 Demonstration of KVH Inc. Firm FOG Products that are used in experiments (a) DSP1500, (b) DSP1750 (Single axis FOG was used) *(Fiber Optic Gyros, n.d.)*

The well-known firms of the gyroscope industry in the world use different types of fiber materials in order to maintain polarization along the fiber. Thus, many errors due to polarization extinction are eliminated. A most common type of PM fiber is panda PM fiber because it is easy and cheap to produce. The other type is bow-tie PM fiber. It is more expensive and arduous to obtain but it is still one of the most used type (Mynbaev & Scheiner, 2001). With the developing material science, e-core (elliptical core) fibers began to be used in fiber optic gyroscopes. In the experiment, two commercial gyroscopes (DSP1500 and DSP1750) whose coil is made of e-core fiber are used.

E-core fiber is mainly produced by the material of acrylate, which is a material in the synthesis of various intermediates that can maintain the polarization of light. Moreover, it is very good insulating material (Wang, Ju, & Jin, 2005).

Test units are these DSP1500 and DSP1750 fiber optic gyros, and the test set-up consists of hardware and software tools listed in Table 4.1.

Table 4.1 Equipment and units used for experiment

Equipment	**Explanation**	**Firm**
KVH DSP 1500	FOG test unit	KVH Industries
KVH DSP 1750	FOG test unit	KVH Industries
NI LabVIEW + PXI (PXI Systems)	Software + hardware that are used for collecting data	National Instruments
MATLAB	Software that is used for analyzing data	The Mathworks, Inc
Espec (Global-N Temperature Cycling Chambers)	Temperature Chamber	Espec North America, Inc.
Rohde & Schwarz Power Supply HMP2030 (HMP4000 Power Supply Series)	Meets the power requirements for test units and PXI tools	Rohde & Schwarz USA, Inc
Test Computer	Includes software tools	-

As software tools, NI LabVIEW (PXI Systems, n.d.) is used for collecting and storing data. Moreover, MATLAB is used for data processing and graphical demonstrations.

As hardware tools, NI PXI Chassis houses PXI modules such as I/O modules which allows to acquire data and build measurements. Other equipment is temperature chamber that allows studying between -70°C and 180 °C.

Figure 4.2 Espec Temperature Chamber *(Global-N Temperature Cycling Chambers)*

The tests are conducted in Espec temperature chamber, which allows programing the desired temperature profile on its touchscreen. It is expected for this kind of chambers that there occur impacts of vibration on the measurements due to fans especially during cooling. Yet, the firm of this test chamber claims that “The condenser is mounted on top with low-speed fans for minimal noise impact.” Even if there are the effects of fans on the measurements, they can be minimized or eliminated by calculations of the mean of output data.

Figure 4.3 Espec Temperature Chamber Touch Screen *(Global-N Temperature Cycling Chambers)*

The temperature profiles are written, controlled and reviewed by the touch screen of the chamber as shown in Figure 4.3. As a result, the overall test set-up is shown in Figure 4.4.

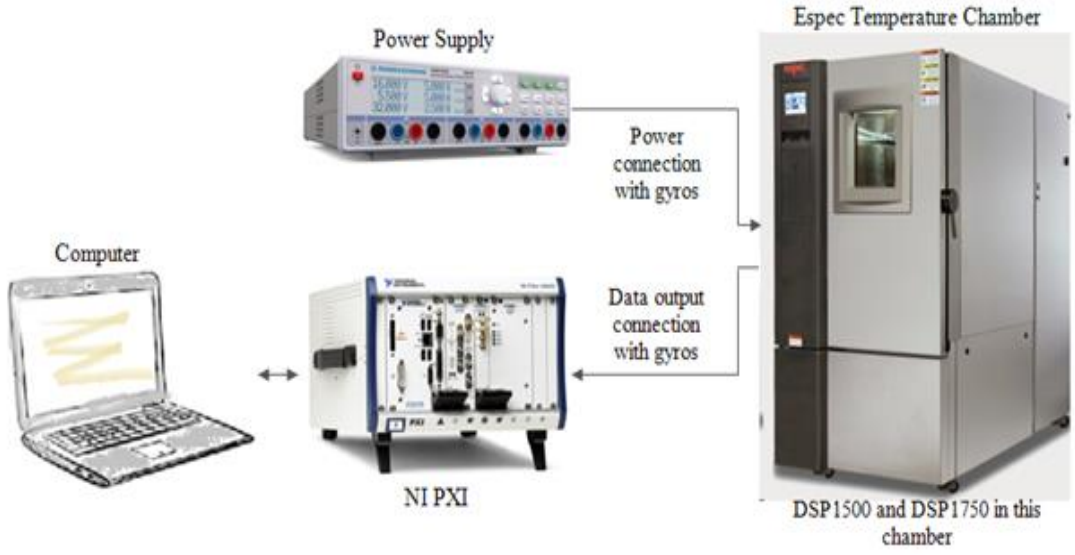

Figure 4.4 Test Set-up Configuration

LabView code for collecting data from KVH gyros is written in the computer, and this code is embedded and run into PXI real-time system, so that gyro output is obtained simultaneously. KVH gyros are placed into the temperature chamber, and their connection cables are passed through a narrow gap on the side of the chamber. After that, this gap is closed, and cables of both gyros are made the related connections with power supply and PXI I/O module. I/O module has RS422 serial electrical interface to communicate with gyros and Ethernet connection with the computer. The power supply is linked with gyros.

The experiments are conducted under two distinct thermal conditions named Profile 1 and Profile 2 as shown in Figure 4.5 and Figure 4.6. Except for these profiles, data was collected from the gyros at room temperature for 12 hours in order to determine bias, bias instability and ARW in stable condition to compare the conditions in Profile 1 and 2.

The Temperature Profile 1 is aimed to observe how the gyros behave during temperatures that change gradually. This profile lasts about 19 hours. There are various temperature values that the gyros are exposed, but the rate of change between two different temperatures is fixed at 5º/min. The Temperature Profile 1 scans through the range of the operating temperatures of the gyros by waiting at every temperature for 1 hour. The scanning temperatures are 20°C, 10°C, 0°C, -10°C, -20°C, -30°C, -40°C, -30°C, -20°C, -10°C, 0°C, 10°C, 20°C, 30°C, 40°C, 50°C, 60°C, 70°C respectively.

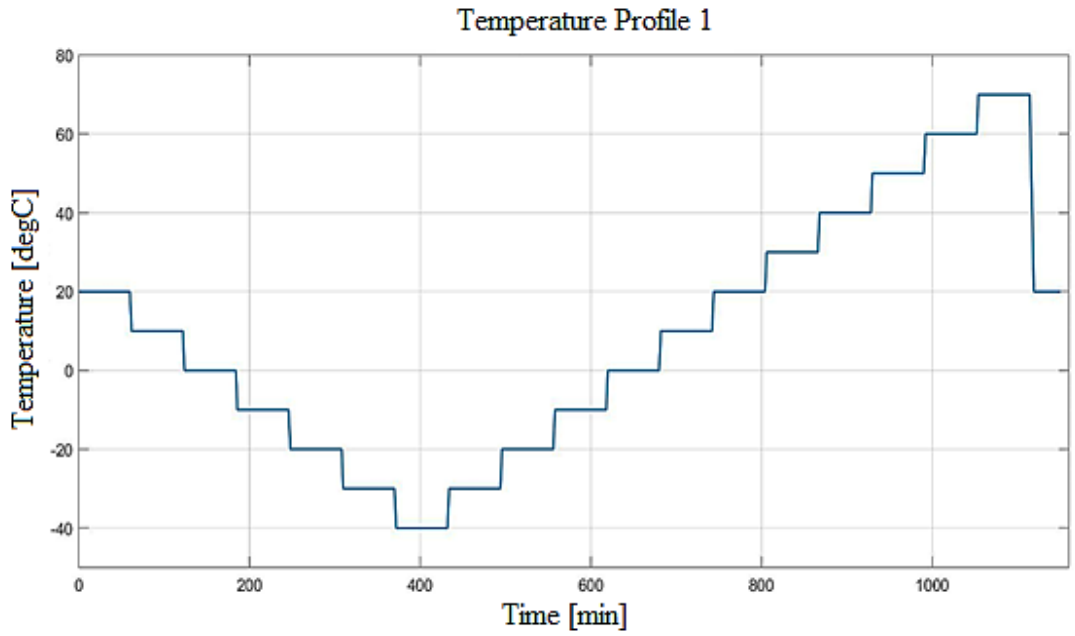

Figure 4.5 The Applied Temperature Profile 1

The Temperature Profile 2 is aimed to observe how the gyros react during temperatures that change in different rates of temperature. This profile lasts about 18 hours. The rates of change between two fixed temperatures which are -40°C and 70°C differ ±2°/min, ±4°/min, ±5°/min and ±8°/min respectively.

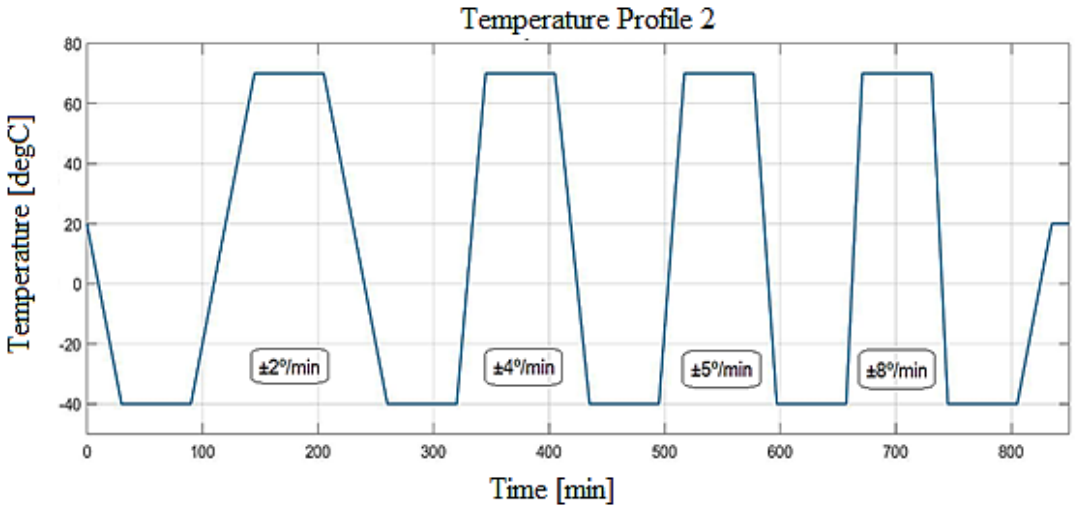

Figure 4.6 The Applied Temperature Profile 2

Espec temperature chamber is capable of operating temperature change rates maximum ±8º/min. That is why the temperature rates of ±2º/min, ±4º/min, ±5º/min and ±8º/min are used in Temperature Profile 2.

Unfortunately, the temperature chamber has no recorder; hence, the applied temperature profiles could not be transferred in a computer environment. As a result, the photograph of the display image, which is in front of the chamber, was taken to be illustrated as Figure 4.7.

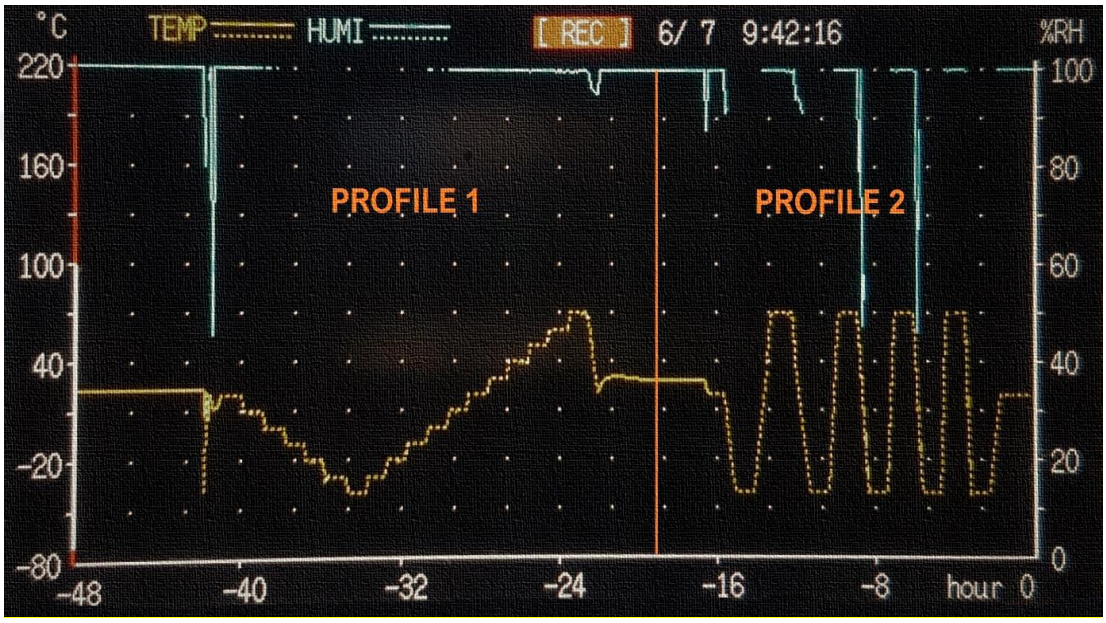

Figure 4.7 Espec display image that applied temperature profiles are demonstrated (yellow line refers to changing temperature with respect to time in hour, x-axis shows time counting backward, and first y axis is temperatures in degree Celsius)

According to Profiles 1 and 2, the "Allan Variance" graphs were plotted to show bias instability and ARW for the room temperature, Profile 1 and Profile 2. In the Allan variance graph, the bias instability is calculated from the region of the slope of “0” and the ARW is calculated from the region of the slope of -1/2 (Allan Variance: Noise Analysis for Gyroscopes, 2015) (IEEE Standard for Sensor Performance Parameter Definitions, n.d.).

Furthermore, when gyros at a stationary position, they are affected by Earth rate. In other words, the sensor senses Earth rate and adds up to its output data. Therefore, it is needed to subtract the Earth rate, which is 15.04107°/hr (Lefevre, 2014), from the measured data. In order to calculate the Earth rate in a certain area, the formula "Earthrate=(15.04107)*sin(latitude)" is used (Groves, 2008). For all tests, Earth rate is eliminated from measured data.

All tests are conducted at the stationary position so that angular rate should be seen zero in ideal case. However, rate error is expected at the measurements because of many error sources. These error sources can be both internal and external sources. In this thesis, the only variable during the tests is external temperature. When the external temperature waits at different values and changes with distinct temperature rates, change in rate error is observed. In addition to shupe and Tdot effects that are expected to observe, thermal effects due to electronic noise also appear in ARW because electronic cards of the gyros are used in the test chamber.

The data outputs of DSP 1500 and DSP 1750 under different thermal conditions looks like in Figure 4.8, Figure 4.9, Figure 4.10 and Figure 4.11.

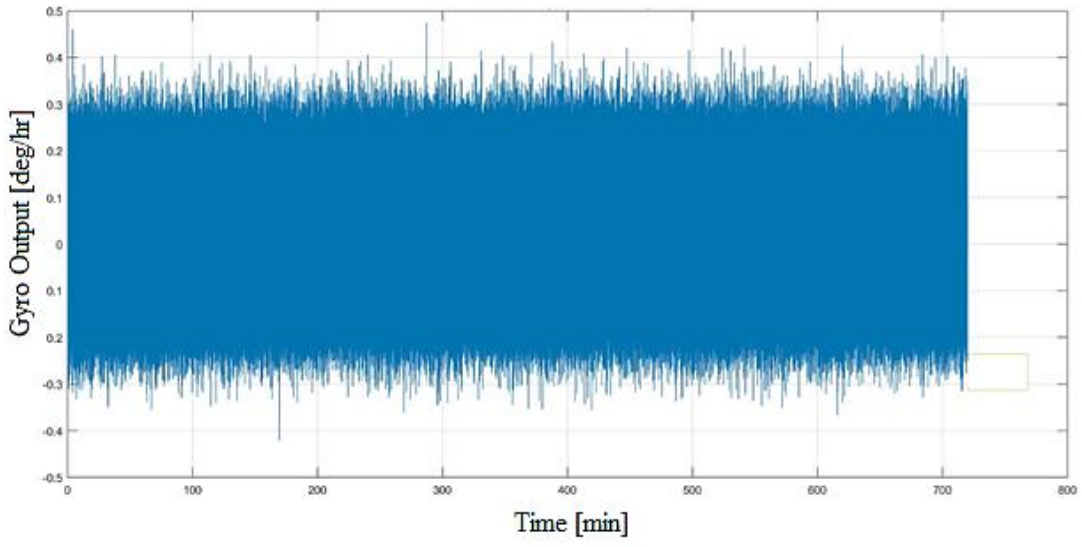

Figure 4.8 The Output of The Gyroscope named DSP 1500 under Room Temperature

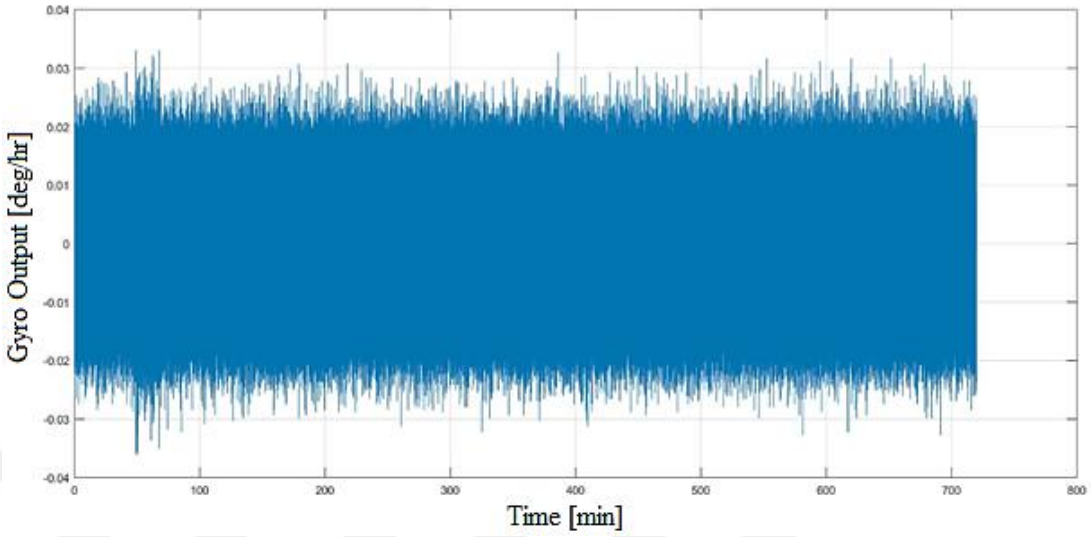

Figure 4.9 The Output of The Gyroscope named DSP 1750 under Room Temperature

In Figure 4.8 and Figure 4.9, outputs of gyros in room temperature have a stable movement in a certain range, so there is not any disparate fluctuation.

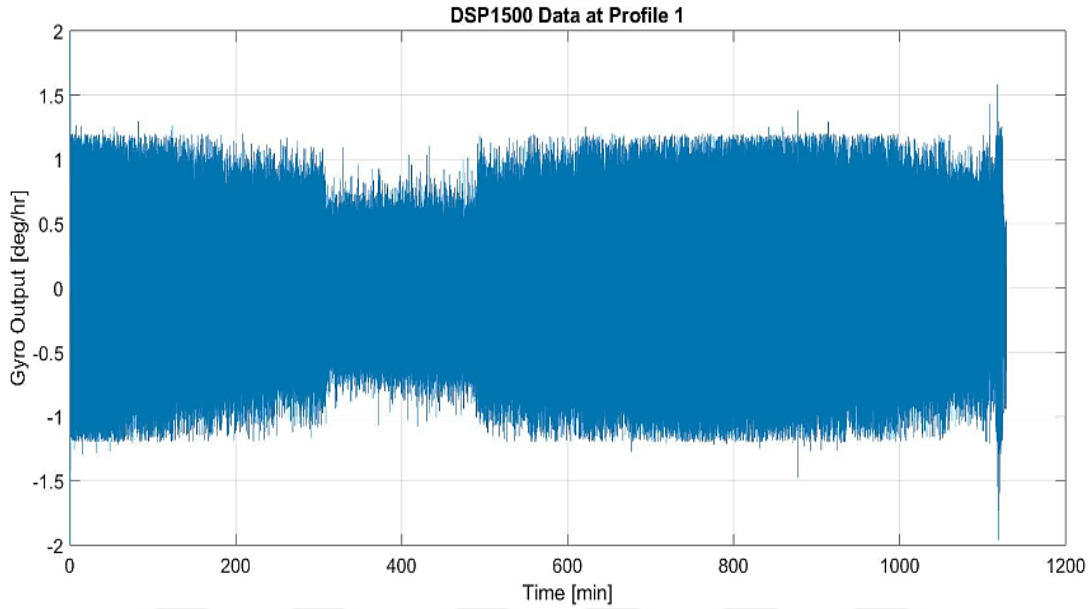

Figure 4.10 The Output of The Gyroscope named DSP 1500 under The Temperature Profile 1

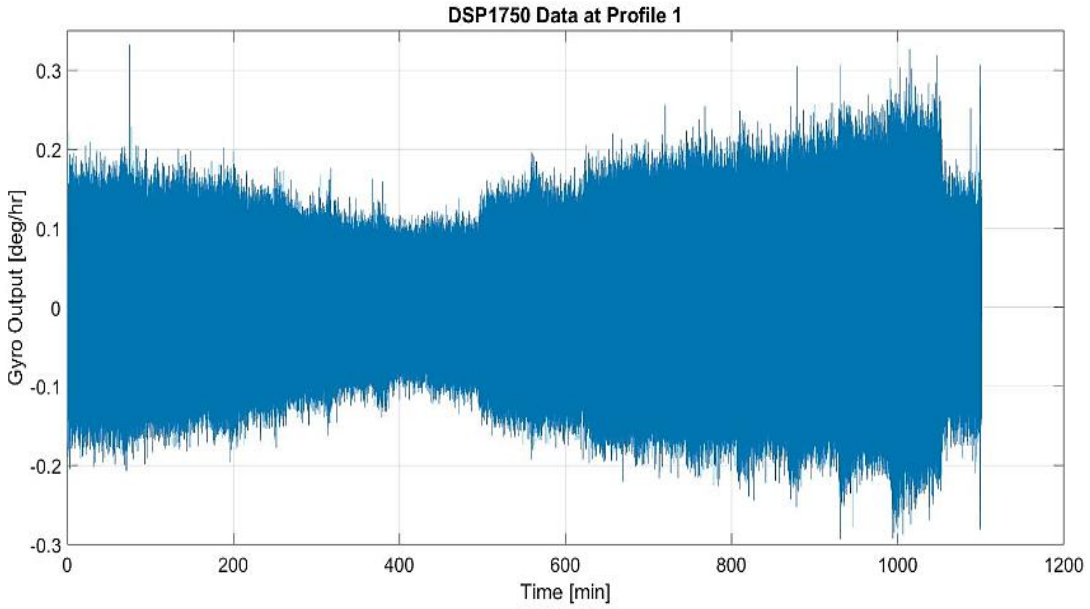

Figure 4.11 The Output of The Gyroscope named DSP 1750 under The Temperature Profile 1

In Figure 4.10 and Figure 4.11, behaviors of both DSP 1500 and DSP 1750 gyros are similar when temperature values decrease and increase systematically. Rate error traces the change in temperature values and fluctuates mainly about high-temperature degrees by comparison with decreasing thermal conditions.

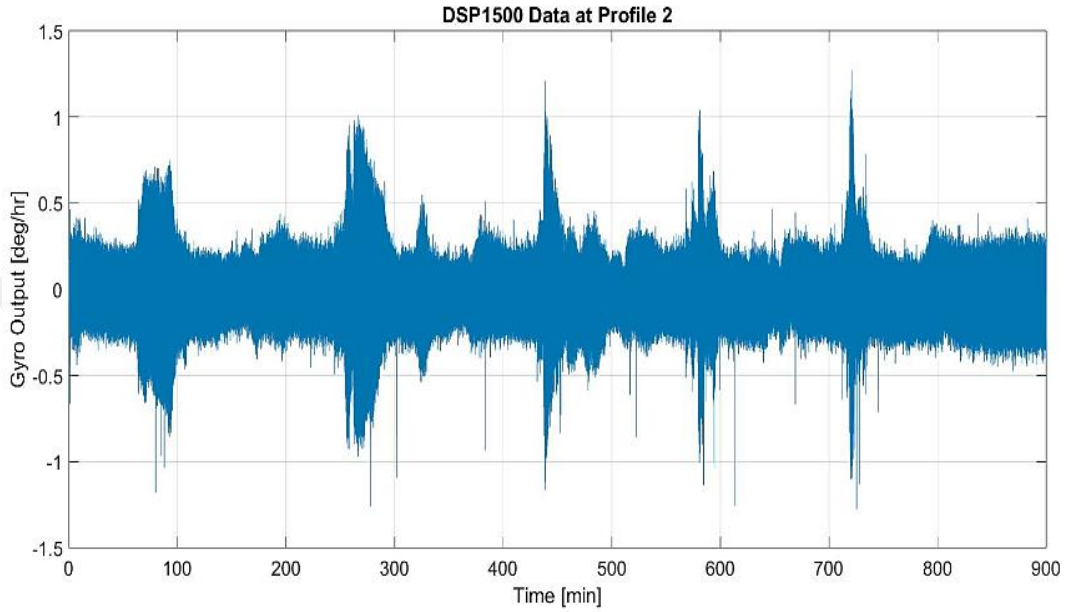

Figure 4.12 The Output of The Gyroscope named DSP 1500 under The Temperature Profile 2

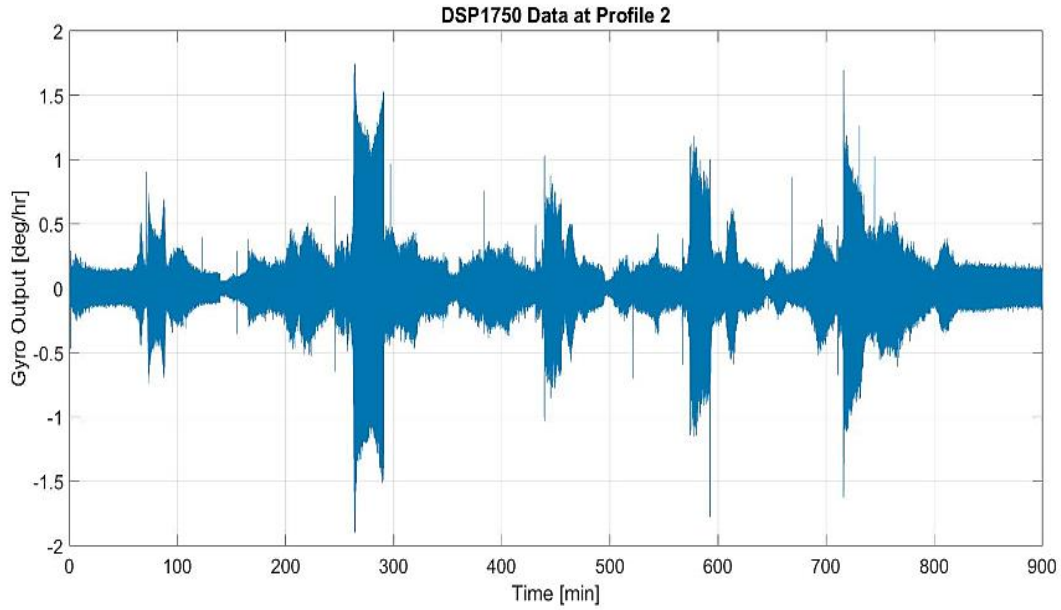

Figure 4.13 The Output of The Gyroscope named DSP 1750 under The Temperature Profile 2

In Figure 4.12 and Figure 4.13, there are distinct fluctuations in output for both DSP1500 and DSP1750 when thermal changes occur. Rate error sharply exists in particular times that correspond to thermal changes are present.

The bias instability and ARW results of DSP1500 and DSP1750 via Allan Variance curves are shown under their thermal profiles below.

In Figure 4.14 and Figure 4.15, Allan variance graphs of gyroscopes named DSP1500 and DSP1750, which wait at room temperature about 12 hours are illustrated respectively. From the graphs, their bias instability and ARW are calculated and noted in Table 4.2 and Table 4.3.

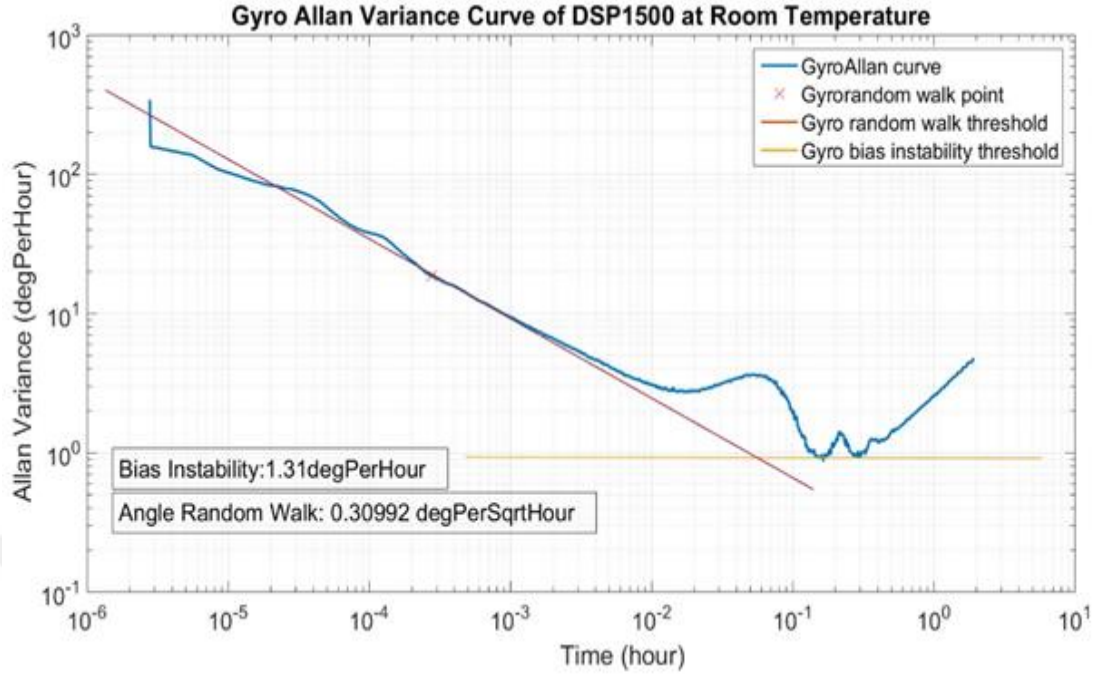

Figure 4.14 Allan Variance Graph of DSP 1500 for Room Temperature

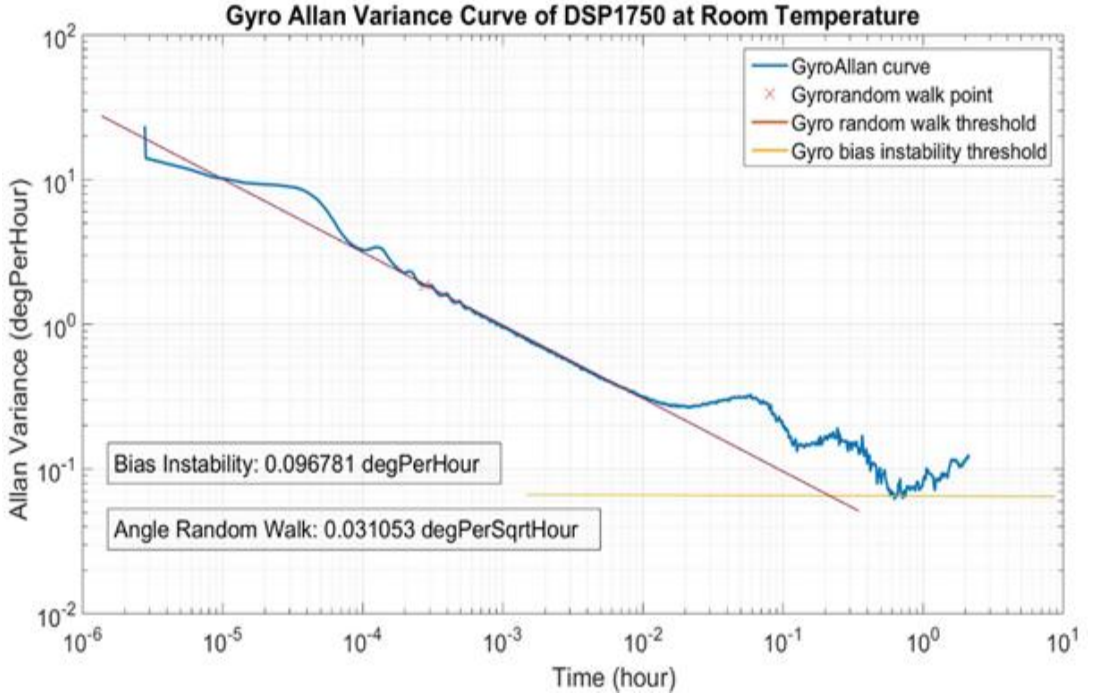

Figure 4.15 Allan Variance Graph of DSP 1750 for Room Temperature

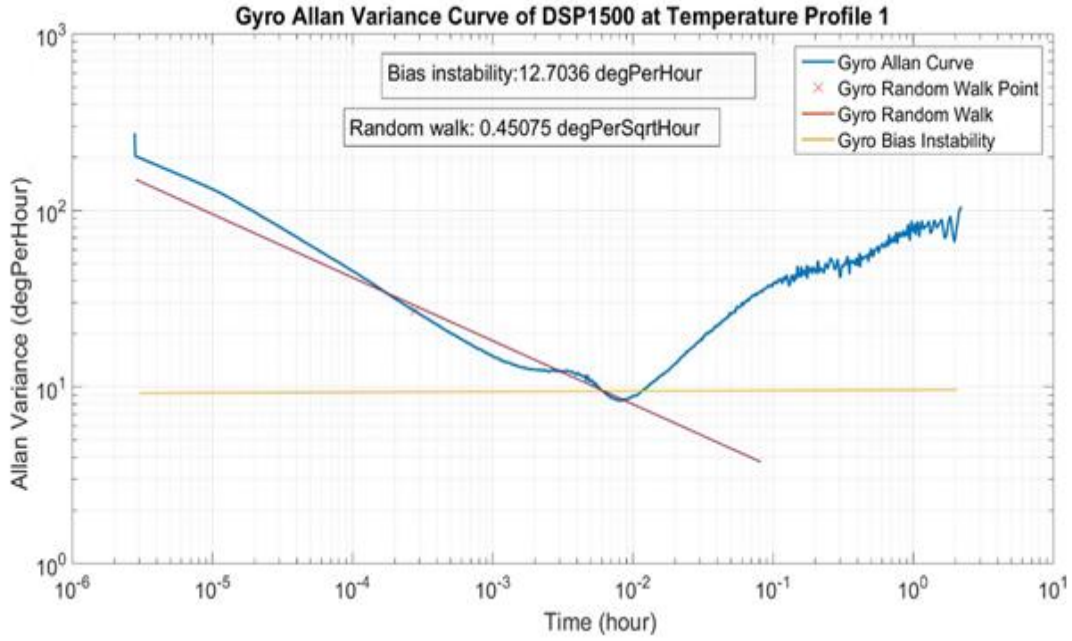

Figure 4.16 Allan Variance Graph of DSP 1500 for Temperature Profile 1

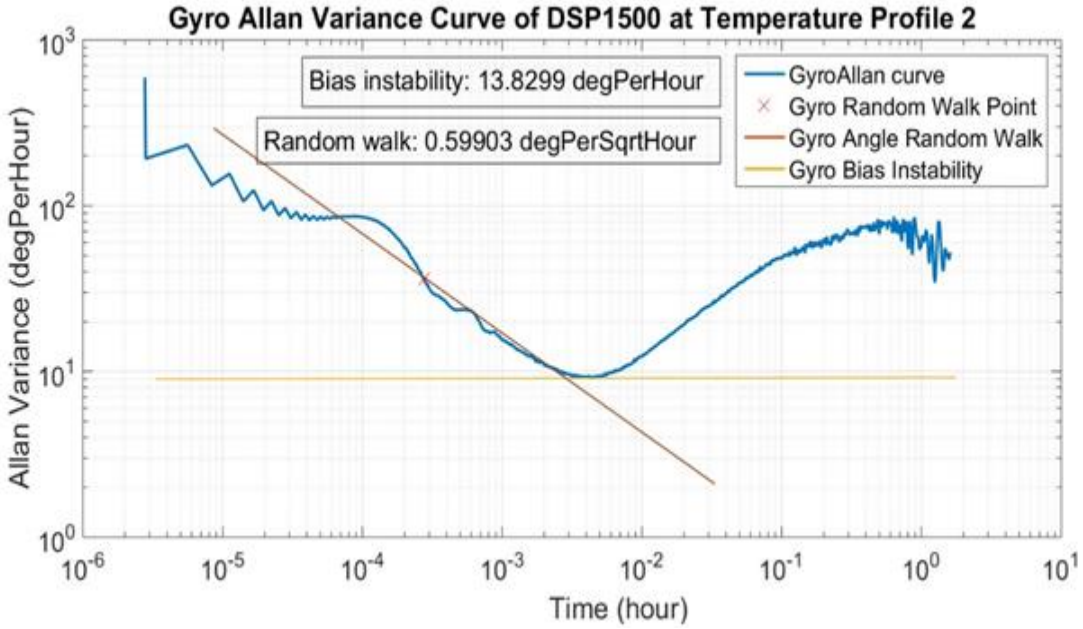

Figure 4.17 Allan Variance Graph of DSP 1500 for Temperature Profile 2

In Figure 4.16 and Figure 4.17, Allan Variance graphs of the gyroscope named DSP1500 at Temperature Profile 1 and Profile 2 are drawn respectively. At these two different temperature profiles, its bias instability and ARW are calculated and noted in Table 4.2.

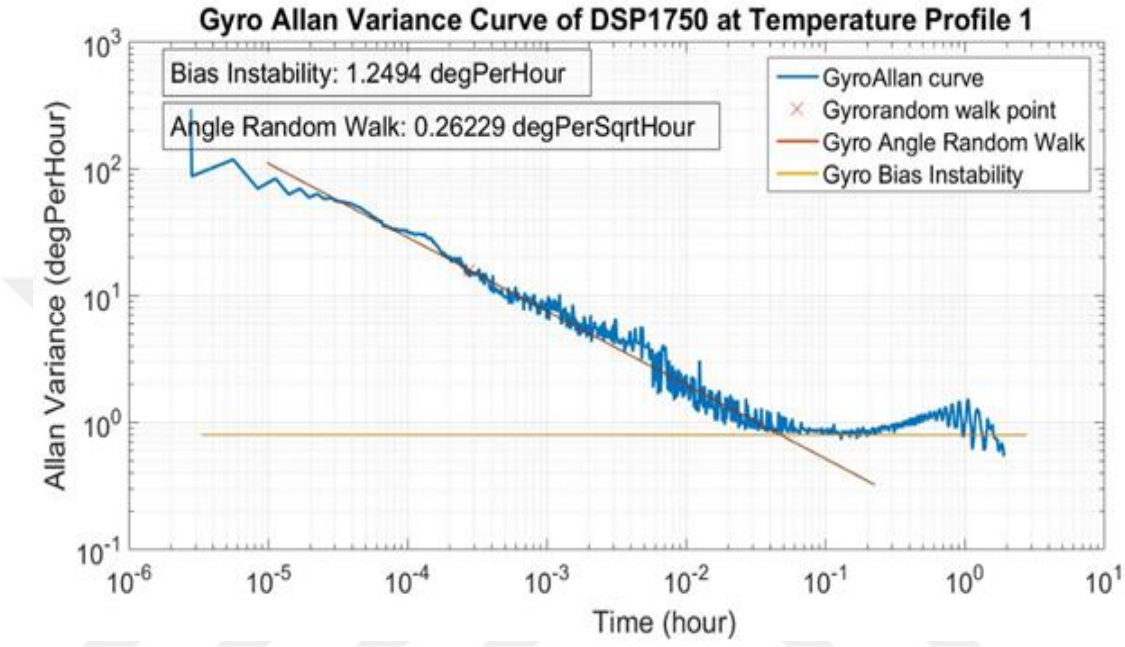

Figure 4.18 Allan Variance Graph of DSP 1750 for Temperature Profile 1

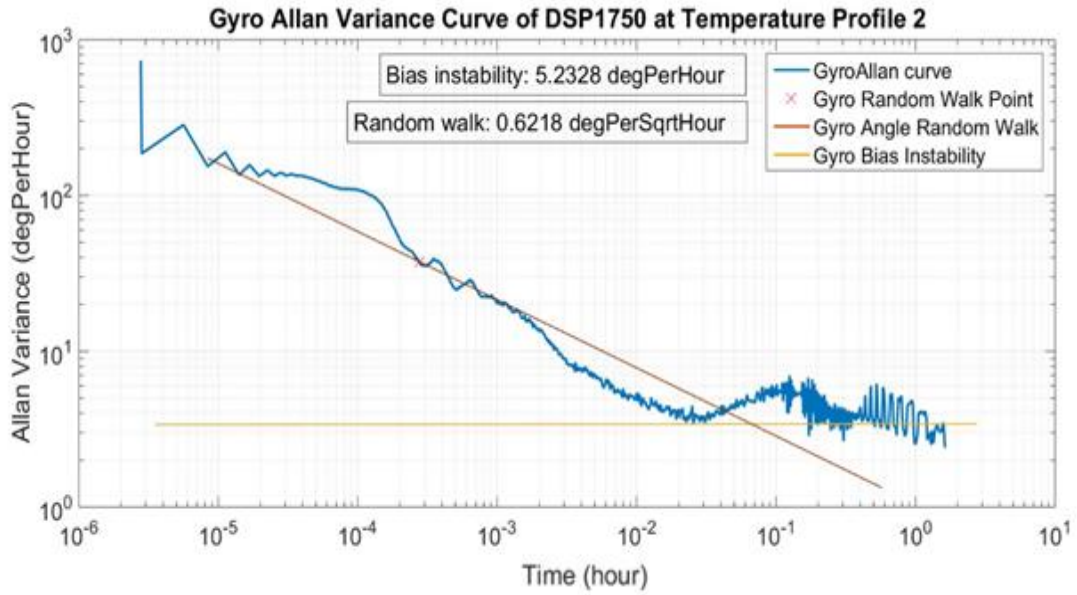

Figure 4.19 Allan Variance Graph of DSP 1750 for Temperature Profile 2

In Figure 4.18 and Figure 4.19, Allan Variance graphs of the gyroscope named DSP1750 at Temperature Profile 1 and Profile 2 are drawn respectively. At these two different temperature profile, its bias instability and ARW are calculated and noted in Table 4.3

Table 4.2 Bias instability and ARW of DSP1500 in different temperature conditions

FOG DSP1500	**At room temperature (25°/C)**	**Profile 1**	**Profile 2**
Bias Instability	1.31°/sa	12.7036 °/sa	13.8299 °/sa
Angle Random Walk (ARW)	0.30992°/$\sqrt{\text{sa}}$	0.45075 °/$\sqrt{sa}$	0.59903 °/$\sqrt{sa}$

Table 4.3 Bias instability and ARW of DSP1750 in different temperature conditions

FOG DSP1750	**At room temperature (25°/C)**	**Profile 1**	**Profile 2**
Bias Instability	0.096781°/sa	1.2494 °/sa	5.2328 °/sa
Angle Random Walk (ARW)	0.0310053°/$\sqrt{sa}$	0.2623 °/$\sqrt{sa}$	0.6218 °/$\sqrt{sa}$

In Table 4.2 and Table 4.3, bias instability and ARW of FOG DSP1500 and DSP1750 are listed for different temperature profiles. DSP1500 is an older version than DSP1750 (Fiber Optic Gyros), hence there are performance differences between them. When they are examined in the aspects of their own characteristics, their residual errors behave similarly under defined temperature profiles. It is observed that their bias instability and ARW increase at Temperature Profile 1 when compared with the test at room temperature. In addition, these errors increase at temperature Profile 2 when compared with the Profile 1. It is expected that rate error should increase at high and low temperatures and during temporal thermal changes due to Shupe effect and Tdot effect (in other words, elasto-optic effect). The test gyros are mostly influenced by Shupe effect in Temperature Profile 1. In Temperature Profile 2, they are mostly exposed to Tdot effect as well as Shupe effect. The rate error accumulates with the effect of thermally induced non-reciprocity although the non-reciprocity is tried to be avoided by symmetrical winding methods. The coils of KVH gyros have been symmetrically wound; therefore, it is expected that Shupe effect, which is sensed at the output due to Temperature Profile 1 and 2, is minimized. Hence, Tdot effect is mostly expected to be observed.

Bias calculation is made by computing the mean data (IEEE Standard Specification Format Guide and Test Procedure for Single-Axis Interferometric Fiber Optic Gyros, n.d.). Bias of DSP1500 at room temperature is calculated as 0.0310 deg/hr, and bias of DSP1750 at room temperature is calculated as 0.0029 deg/hr. In Figure 4.20 and Figure 4.21, bias calculations are made in the aspect of their special temperature conditions. In order to observe the change in bias which has temperature dependency in theory, the whole data of the gyros for each test are divided into small parts. Every part of the data is averaged and saved. Hence, the tendency of bias under thermal changes is obtained by gathering the whole averaged data. The gyros have been already calibrated for the temperature dependency problem. Nevertheless, it is expected to observe that there are still temperature dependent movements of residual data.

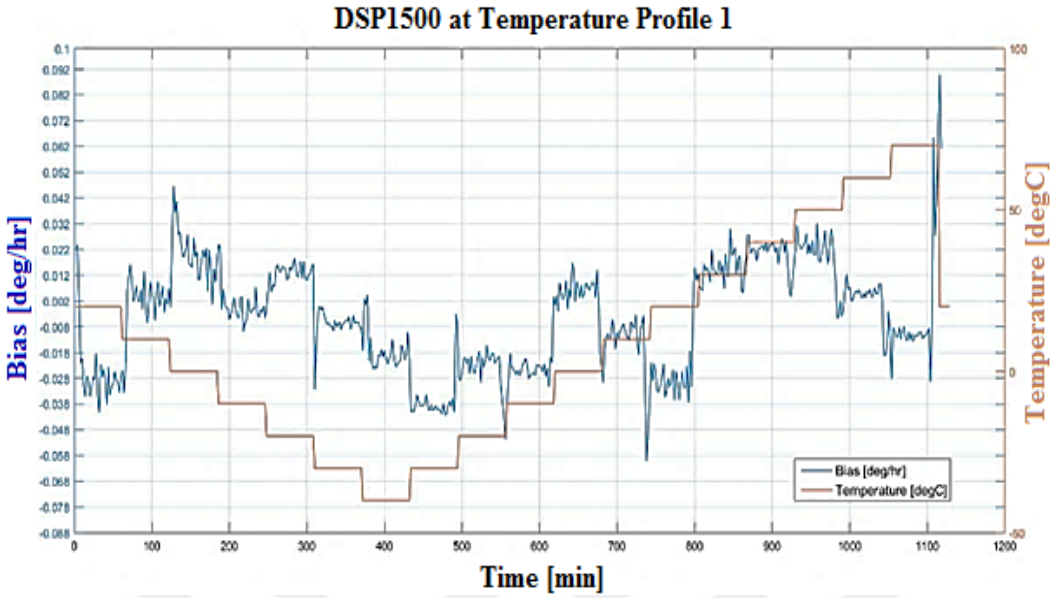

(a)

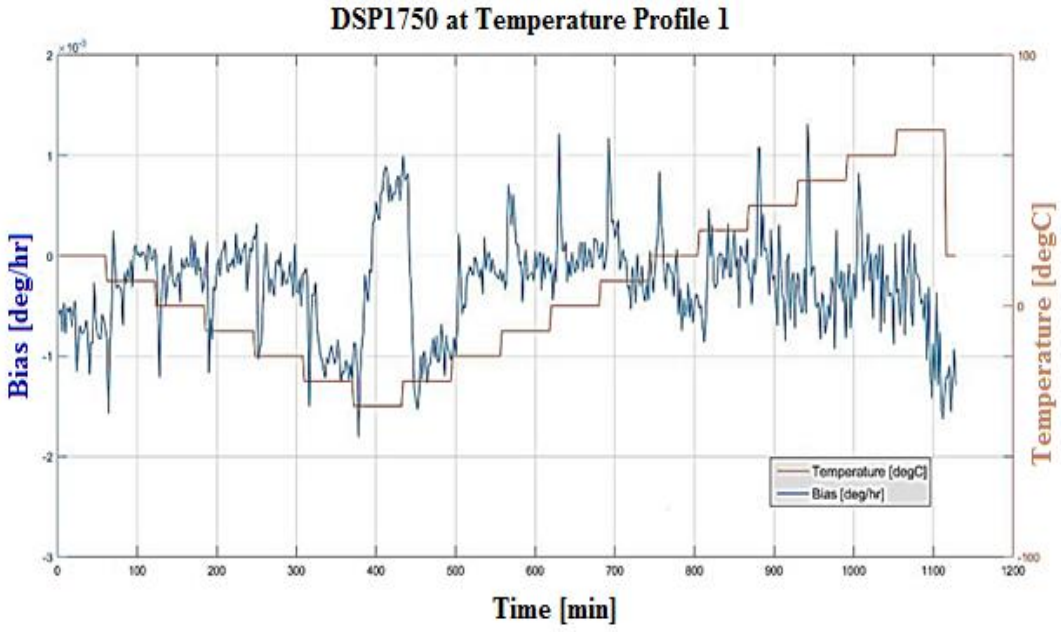

(b)

Figure 4.20 (a) Bias results of DSP1500 at Profile 1, (b) Bias results of DSP1750 at Profile 1

In Figure 4.20, the bias of DSP1500 (a) and DSP1750 (b) is plotted with the Temperature Profile 1 during the test. Bias vs time and temperature vs time graphs are superimposed in order to follow the change in bias with the thermal changes. It is expected that the rate error chases the thermal changes.

Considering the Equation 3.19, if temperature changes in positive direction, the change in bias trends positively or vice versa. In this case, the bias results come from residual errors. It is observed that residual data reacts the thermal changes. Bias of DSP1500 have distinct movements under different temperature steps apparently. DSP1750 has also temperature dependent behaviors. Not totally, but DSP 1500 and DSP 1750 looks like following the thermal changes. There were unexpected bias peaks for DSP1750 at -40°C, which could be caused by any internal or environmental effects. It is needed to know if the test were repeated, would DSP1750 behave the same? Thus, it is hardly said that the behaviors of these residual bias will always be as in Figure 4.20 (a) and (b). In order to be observed how their residual error behaves under systematically decreasing and increasing temperature changes, the test of profile 1 should be repeated numbers of times. Therefore, the residual characteristics of the gyros are well-understood.

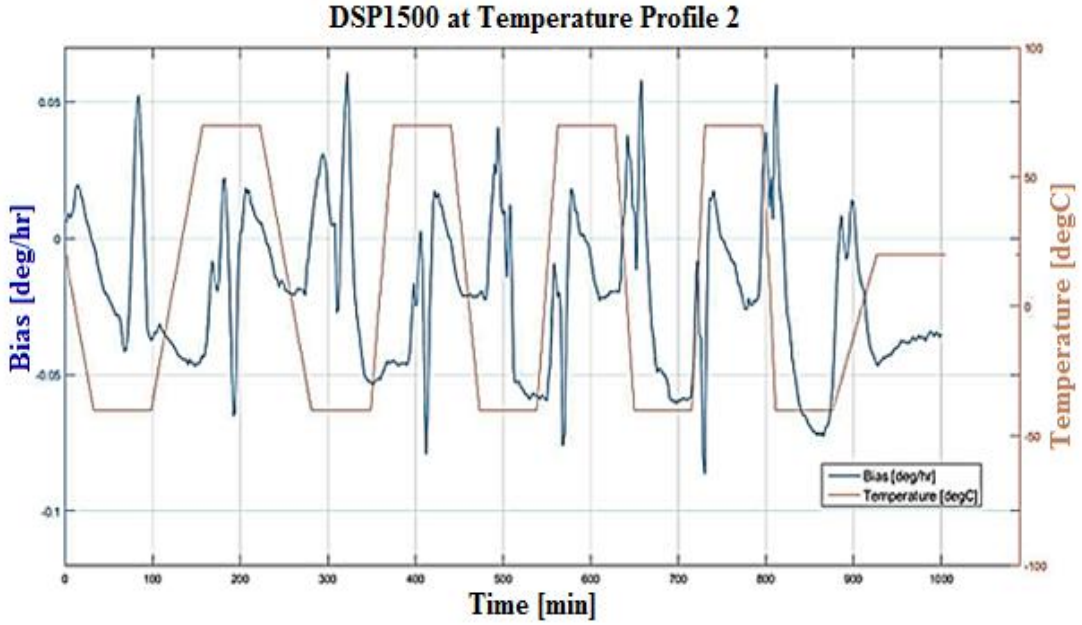

(a)

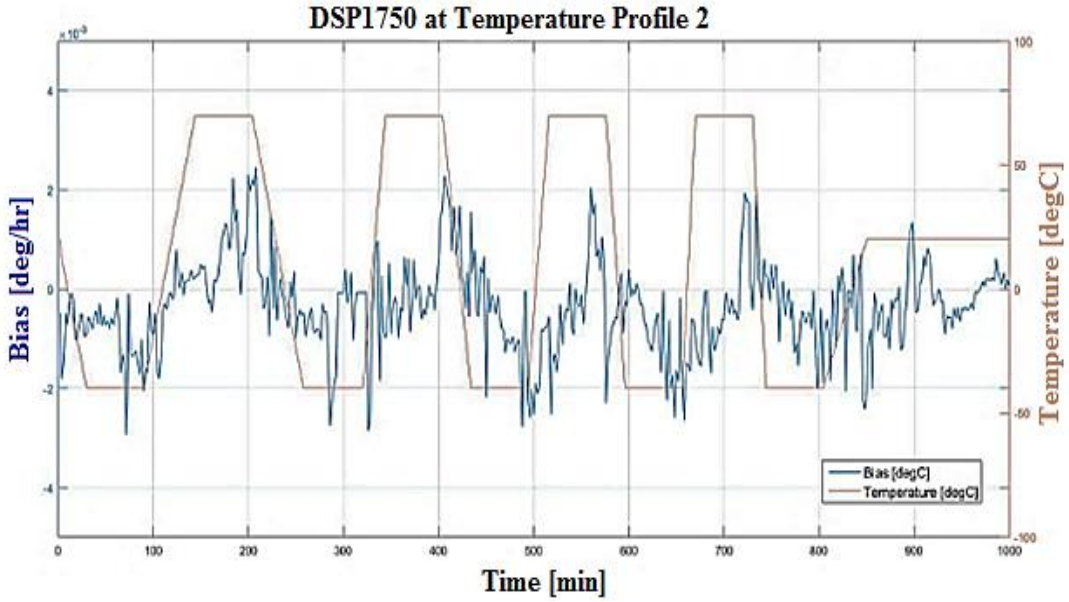

(b)

Figure 4.21 (a) Bias results of DSP1500 at Profile 2, (b) Bias results of DSP1750 at Profile 2

In Figure 4.21, bias change vs time graph of the gyros DSP 1500 and DSP1750 are plotted with Temperature Profile 2. It is seen that the residual bias changes with the thermal changes proportionally as expected. In Temperature Profile 2, the elasto-optic effect (or Tdot effect) mostly influences the rate error of gyros. Therefore, change in bias has more explicit behavior with the thermal profile. It is expected by means of the Equation 3.19 that the Tdot effect can be modeled easily rather than Shupe effect (Lefevre, 2014).

In Figure 4.22 and Figure 4.23, three-dimensional graphs are plotted by using the parameters of measured bias, temperature rate of change noted as Tdot in the graphs and temperature values. The purpose is to observe the trend when temperature changes in different rates operated in Profile 2, how the bias of gyros are influenced. In addition to this relation, the bias data obtained from different temperatures operated in Profile 1 is also added to enrich the observation. Therefore, data from both Temperature Profile 1 and 2 are gathered to observe the temperature dependency of bias.

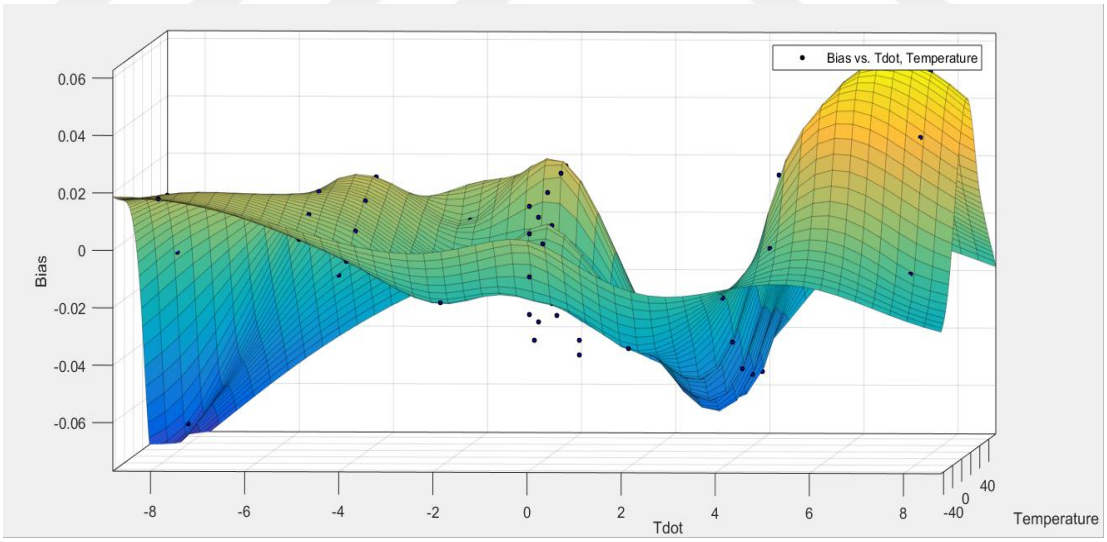

Figure 4.22 Bias [°/hr] vs Tdot (dT/dt) [°C/min] vs Temperature [°C] Graph of DSP1500

In Figure 4.22, when bias and time-dependent temperature changes (Tdot) are compared, it is seen that bias increases with accelerating temperature rate of changes. The change in bias varies in the range of ±0.06 deg/hr. The trend in bias increases in a positive direction when temperature ramp rate increases. Furthermore, it increases in the negative direction when temperature ramp rate increases as expected via the Equation 3.19. Thus, the maximum bias change is seen at -8°/min and +8°/min as expected. Although this gyro is calibrated by its firm, residual data still shows the behavior of bias drifts with temperature changes.

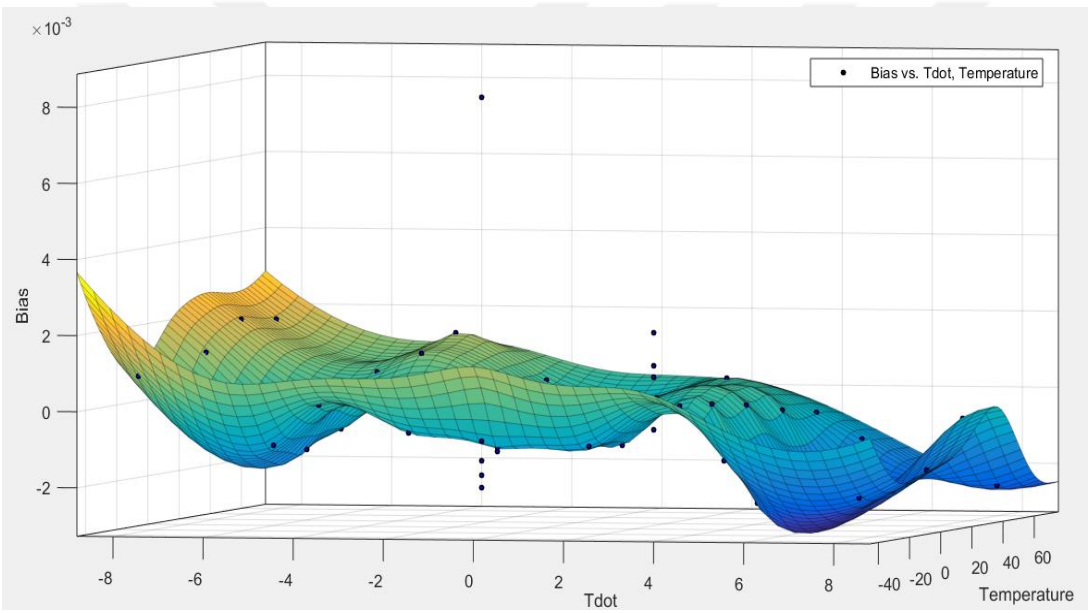

Figure 4.23 Bias [°/hr] vs Tdot (dT/dt) [°C/min] vs Temperature [°C] Graph of DSP1750

In Figure 4.23, when bias and time-dependent temperature changes (Tdot) are compared, it is seen that bias changes with changing thermal rate of changes. The change in bias varies in the range of 0.004 deg/hr and -0.003 deg/hr. Bias drifts as expected when it is compared to its behavior at room temperature; however, the

change in this residual bias is not similar to the previous graph plotted for DSP1500. When temperature ramp rate increases in positive direction, the bias is expected to drift inclines to the positive increments. However, a decline in the trend of bias is observed in Figure 4.23. Nevertheless, it can be realized that there is an influence on bias when changing thermal condition. The reason why proportional change between bias and rate of change in temperature is not seen is the fact that DSP1750 is well-calibrated and upgraded version rather than DSP1500.

CHAPTER 5

SIMULATION OF THERMAL DEPENDENCY OF FIBER COIL

For the simulation, Comsol Multiphysics version 5.3a software is used to model thermal changes in a fiber coil by using Finite Element Analysis Method. Comsol is capable of doing physical analysis, numerical simulations and providing visual applications. By identifying the boundary conditions of a generated geometry, conduction theory, which has already embedded in Comsol "Heat Transfer Module", is used in order to simulate the heat transfer from one end to the other side. Therefore, heat transfer rate can be calculated, simulated, and the distribution of thermal effects can be visualized point by point on the simulated geometry.

In this thesis, the heat transfer module is used, so that the temperature distribution under different thermal conditions can be observed. From Comsol, the output of the temperature changes and refractive index changes can be obtained.

Thermal expansion of fiber material, which causes the change of refractive index at its expanding area is related to some constants: Young modulus (modulus of elasticity), the transverse area, Poisson ratio and the expansion coefficient of fiber material (Zhang, Z. & Yu, F., 2017). For the simulation, parameters for the property of material and dimension of coil are given in Table 5.1 and Table 5.2.

Table 5.1 Material Properties

Materials	Constants	Symbol	Values	Units
Fiber core	Thermal conductivity	σ	1.38	W/(K.m)
	Young modulus	Ecore	1.4	GPa
	Poisson ratio	M	0.17	1
	Expansion coefficient	A	0.5×10^{-6}	1/K
	Stress-optic constants	a_{11} and a_{12}	0.121 and 0.270	1
	Thermo-optic coefficient	dn/dT	~1.0 x 10^{-5} (changes with temperature)	1/K
	Specific heat	c	703	J/(kg.K)
	Density	ρ	2203	kg/m^3
Fiber coating	Young modulus	Ecoating	24.5	MPa
	Thermal conductivity	σ	0.21	W/(K.m)
	Specific heat	c	1400	J/(kg.K)
	Density	ρ	1190	kg/m^3
Mumetal	Thermal conductivity	σ	221	W/(K.m)
	Specific heat	c	896	J/(kg.K)
	Density	ρ	2740	kg/m^3
Adhesive material	Density	ρ	970	kg/m^3
	Specific heat	c	1600	J/(kg.K)
	Thermal conductivity	σ	0.21	W/(K.m)

Table 5.2 Model Parameters

Parameters	Values	Units
Length of fiber (L)	~1109	m
Average diameter of coil (D)	6.6577	cm
Inner coil diameter (R)	4.0037	cm
Total number of Loop/ Layer	88/75	-
Core/coating diameter	8/170	μm

In the simulation, two-dimensional geometry of fiber coil is studied. This geometry is estimated by considering the dimensions of the real products and modeled. Vertical-sectional region of fiber coil is modeled to observe radial and axial temperature stresses. In geometry, there can be seen two regions of fiber material which can be named as left and right cross-sections. If the geometry is revolved in the middle of the coil on vertical axis, one can obtain three-dimensional coil. Dimensions of fiber coil are shown as follows.

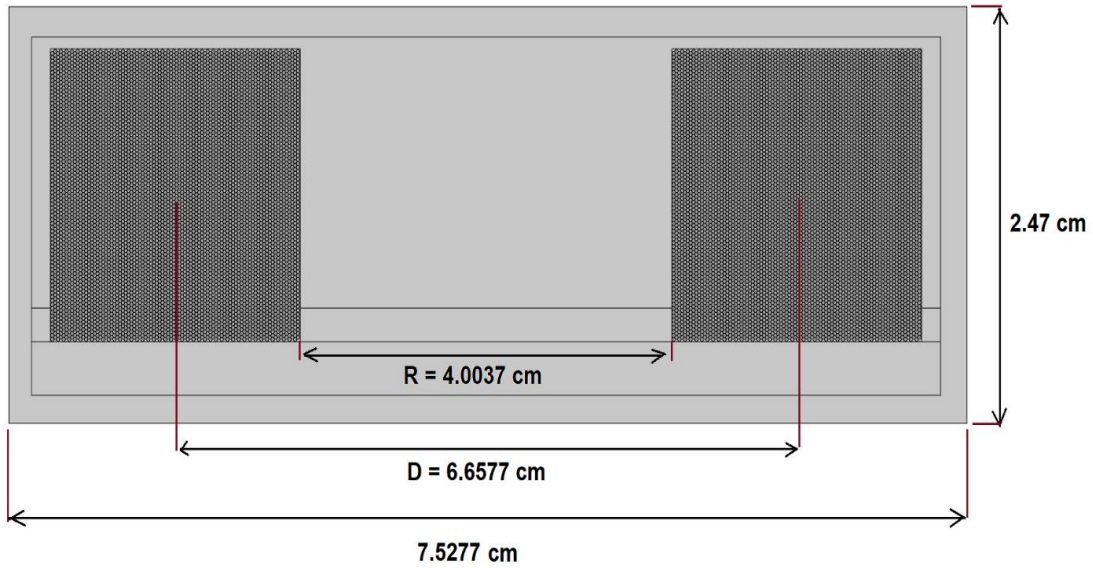

Figure 5.1 Coil Dimensions

The outer dimension of coil geometry in simulation is 2.47 cm x 7.5277 cm (height x diameter). The average diameter of fiber coil (D) is 6.6577 cm, and the distance between the inner coil (R) is 4.0037 cm.

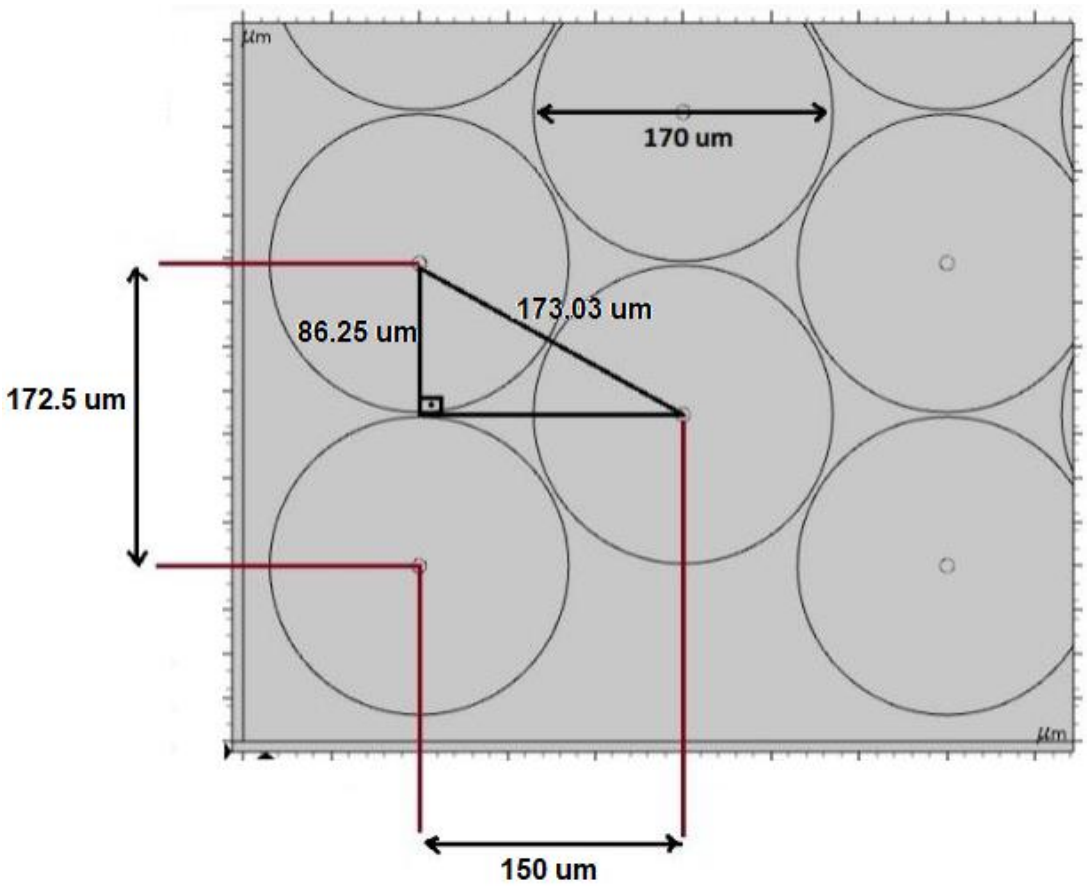

Figure 5.2 Fiber dimensions in the simulation

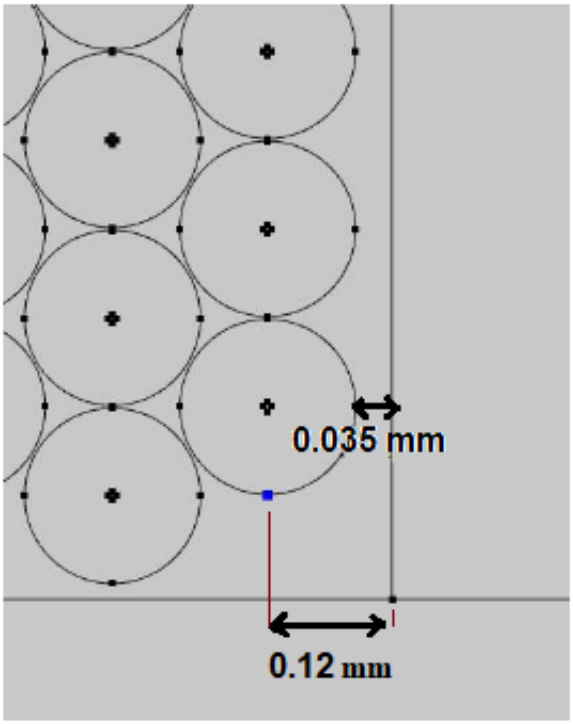

Figure 5.3 Dimension of the fiber covered by the adhesive material in simulation

The fiber length is calculated in the geometry of simulation using the values on Figure 5.1, Figure 5.2, Figure 5.3 and Figure 5.4.

$$L_1 = T \,.\, \pi \,.\, (R + d_c + 2.s) \tag{39}$$

where L_1 is the length in first layer, T is the number of turns, R is the diameter of the inner coil (R = 4.0037 cm in simulation), d_c is the diameter of coating (d_c = 170 μm) and s is the distance from fiber to end of adhesive material (s = 0.035 mm).

$$L_{total} = L_1 + \sum_{i=2}^{N} M.\pi\,(R + 2\,.\,0{,}88235\,.d_c\,.i) \tag{40}$$

where L_{total} is total length of fiber in the coil, M is the number of layer, i is the integer number. The number of 0,88235 multiplied by d_c is as shown in Figure 5.4.

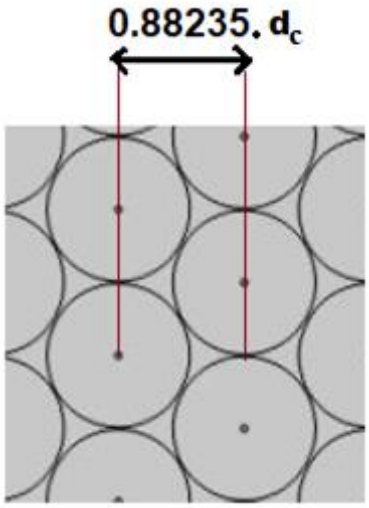

Figure 5.4 The distance between centers of two fibers next to each other

Hence, the length of the coil can be calculated as approximately 1109 m from calculations. In geometry, materials are selected and placed as shown in Figure 5.5.

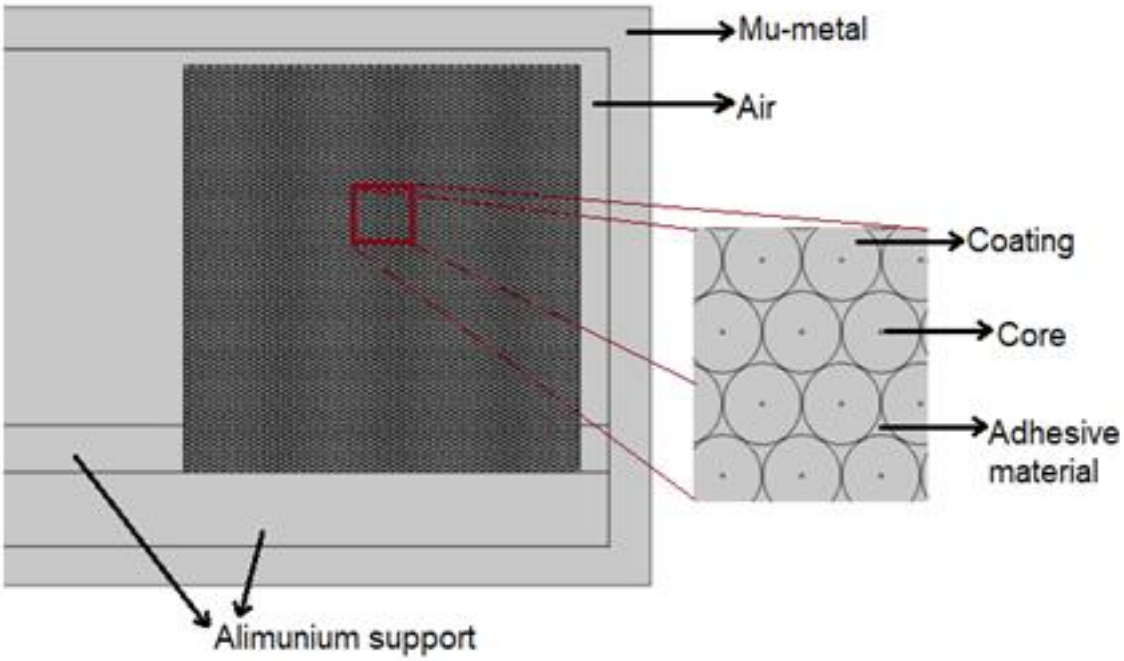

Figure 5.5 Coil Materials

In the simulation, after geometry is build up, materials of regions are specified. Because silica has temperature dependency, Equation 3.2 is inserted as an analytical function into the material property in the model. Defining the physics part of heat transfer module is important because boundary conditions and behaviors of temperature is determined in this part. Besides, characterizing mesh for all region is significant in order to obtain accurate solutions statistically. In simulation, free triangular mesh is used, and different mesh sizing property is applied on every material. Mesh architectures are illustrated in Figure 5.6, Figure 5.7 and Figure 5.8.

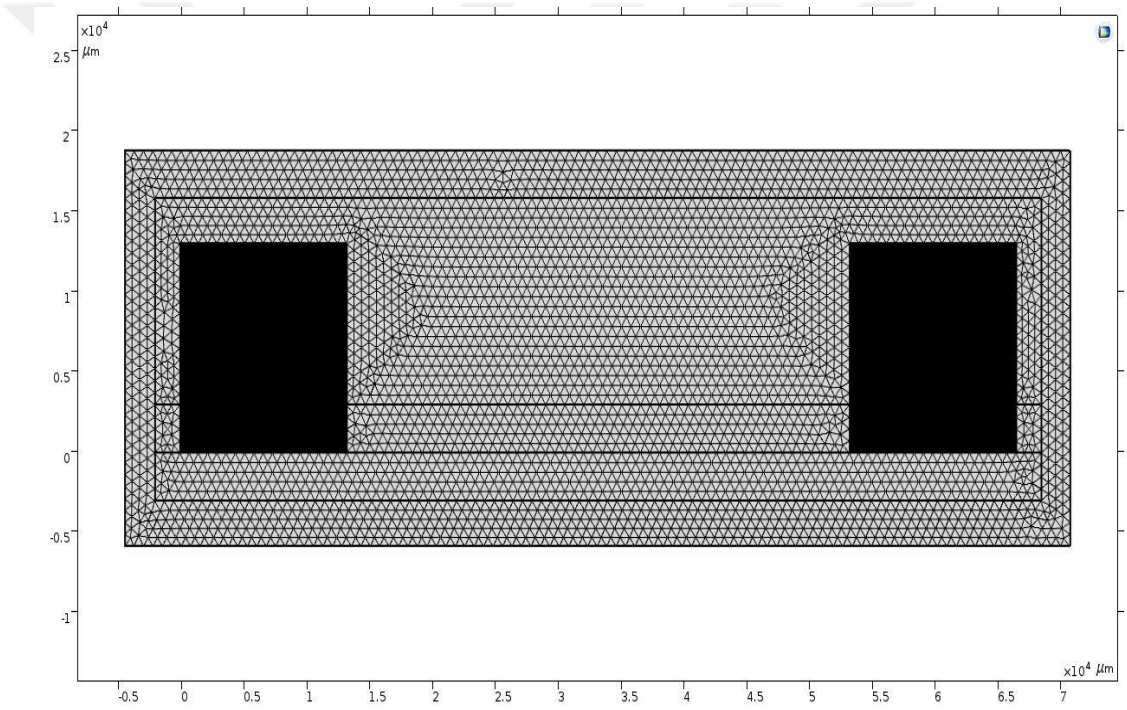

Figure 5.6 Mesh for all system

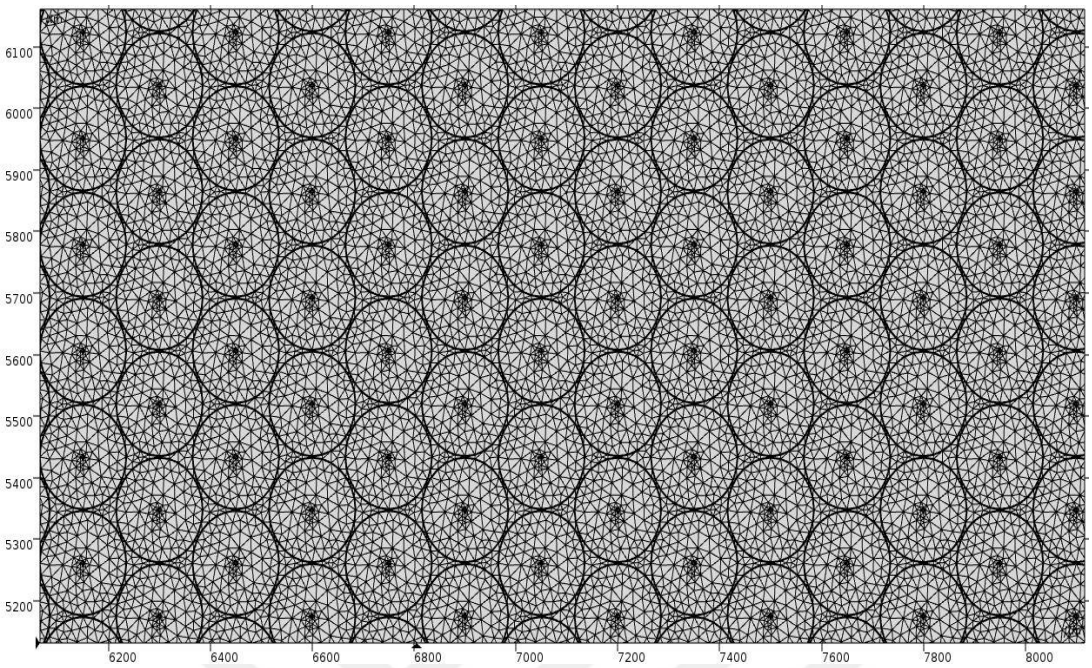

Figure 5.7 Mesh for fibers and adhesive material

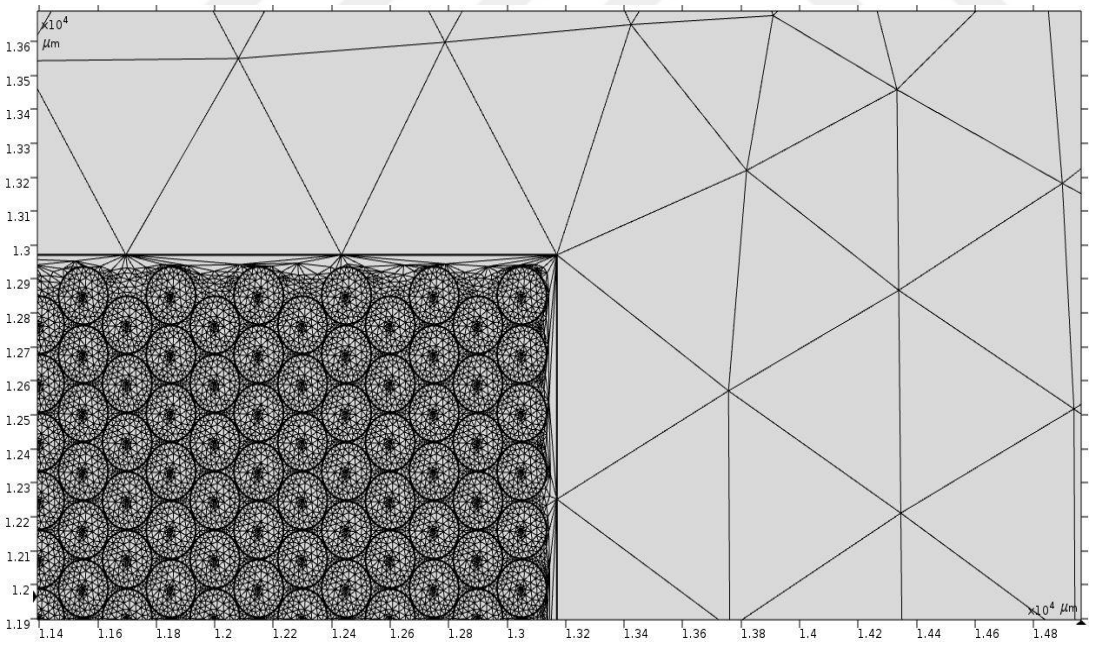

Figure 5.8 Mesh interactions between materials

Simulations are run in the time-dependent study. There are two simulations for both temperature Profile 1 and Profile 2. The simulations conclude data for every 8 minutes up to the end of the simulation for Temperature Profile 1 and for every 5 minutes for Temperature Profile 2.

After run of the simulation, considering quadrupole-wound-coil, data set in Comsol can be generated at the one part of the coil for analysis. If the winding scheme, which is planned to study, is examined carefully, it is sufficient to observe CW and CCW light beams located at the equidistant from the midpoint of coil.

Assuming the fiber coil is wound symmetrically, the symmetric points on the model are selected to study on them in order to see how temperature gradient behaves on them at the same time.

Diffusivity of thermal behavior can be observed at the desired point on the geometry and at the desired time. As an example, four images in simulation are illustrated for four different selected times in Temperature Profile 2.

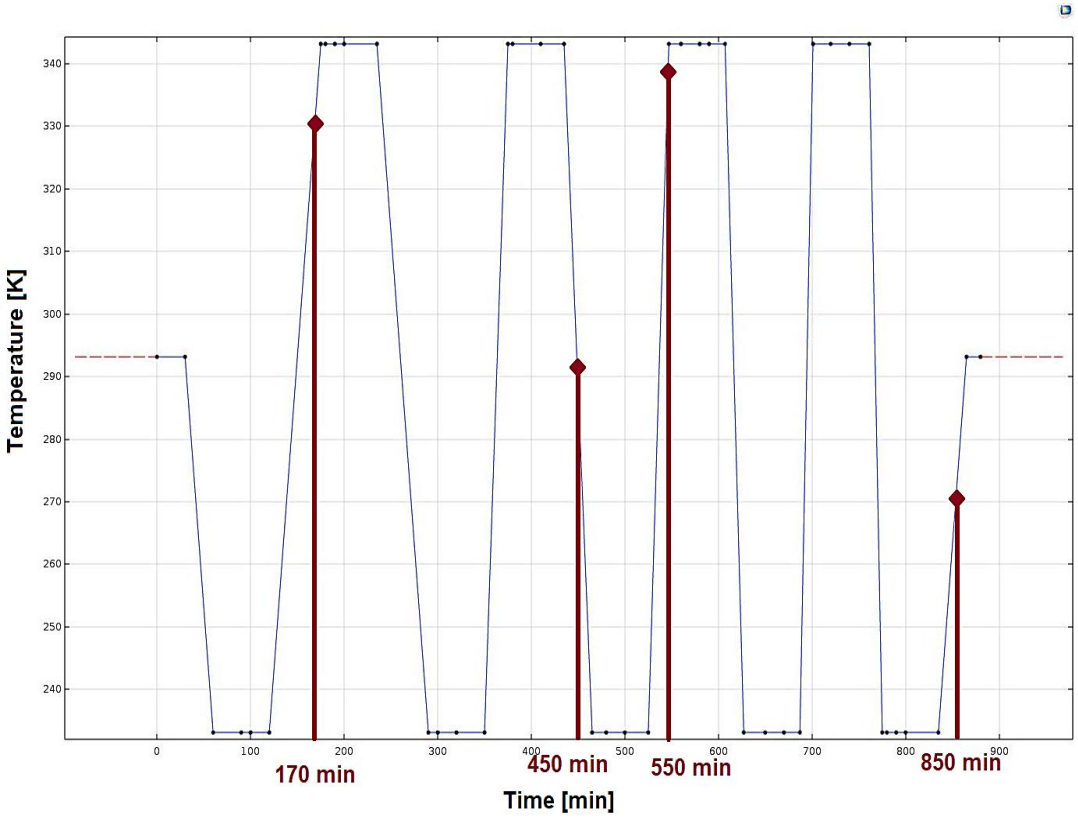

Figure 5.9 The graph of temperature profile 2 and four randomly selected points

From the selected time points, the thermal changes in the fiber coil is simulated and visualized as shown in Figure 5.10, Figure 5.11, Figure 5.12 and Figure 5.13. The color label at right of the figures shows the range of thermal changes.

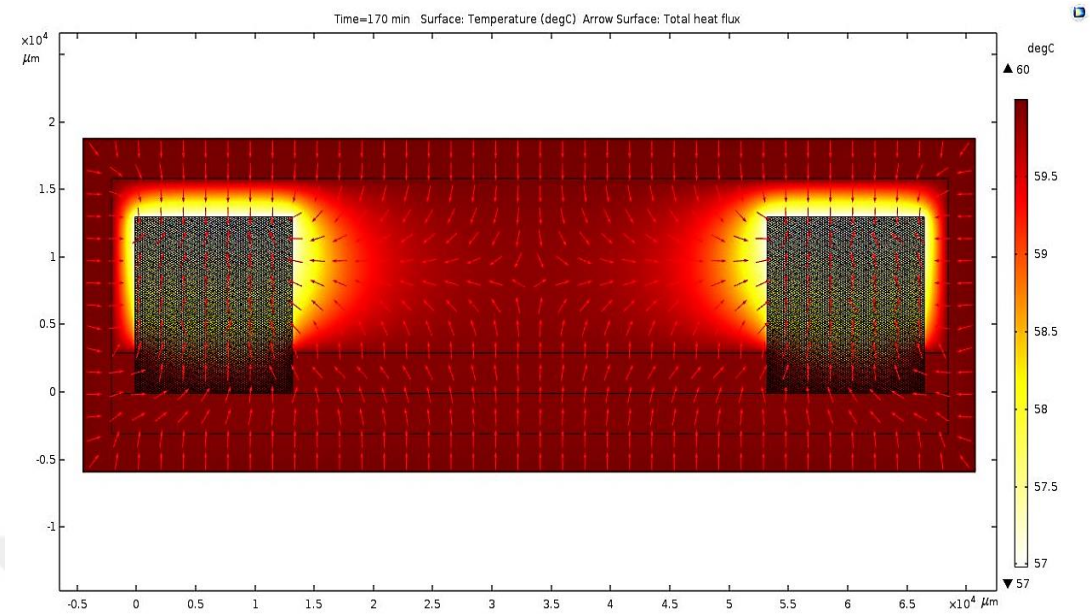

Figure 5.10 The temperature distribution at 170th min for Temperature Profile 2

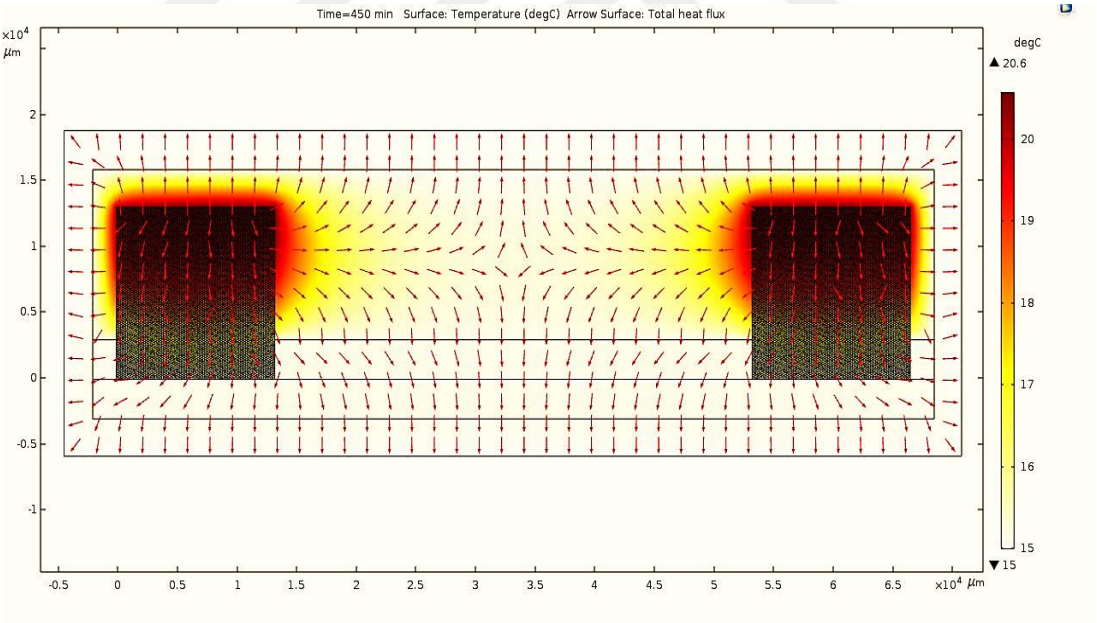

Figure 5.11 The temperature distribution at 450th min for Temperature Profile 2

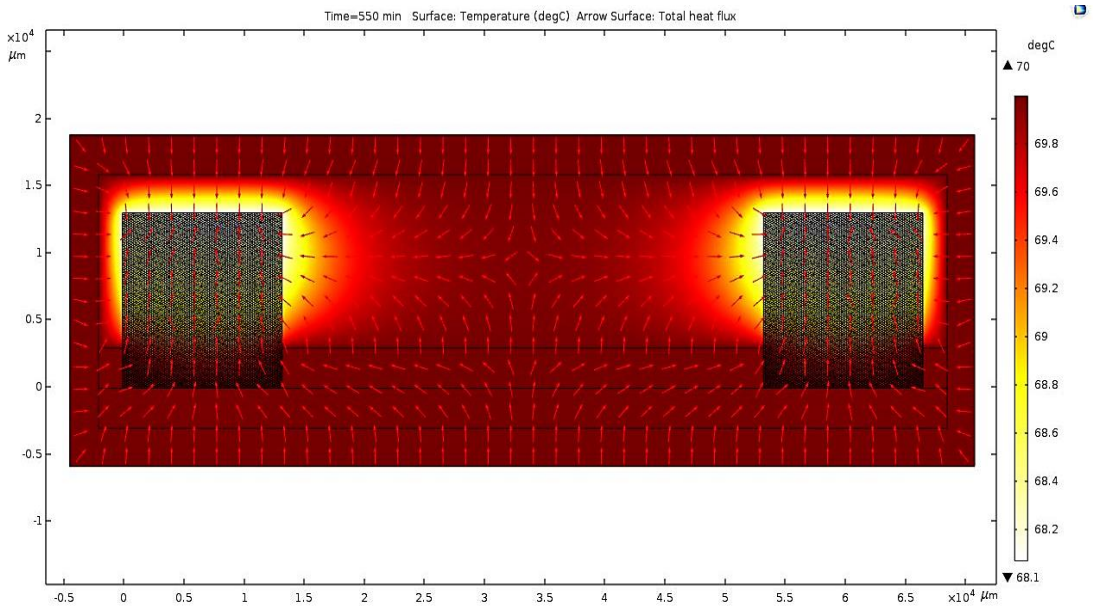

Figure 5.12 The temperature distribution at 550th min for Temperature Profile 2

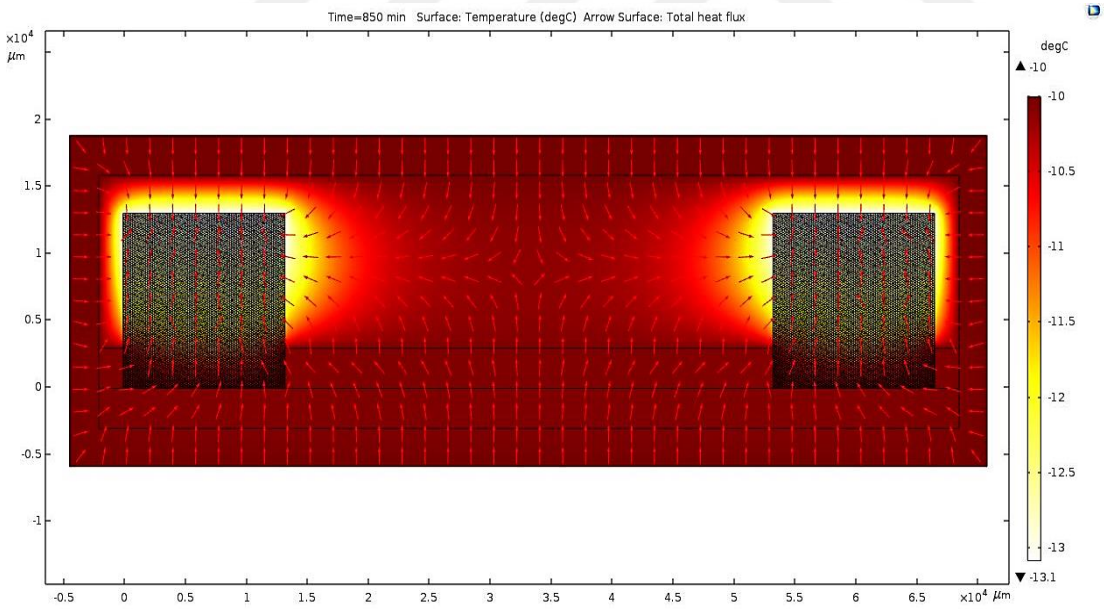

Figure 5.13 The temperature distribution at 850th min for Temperature Profile 2

One can click on the point of the geometry that is desired to study in order to see what the temperature is on that point at that time.

Although this simulation is two dimension, it can reflect how temperature transfers in every fiber in the coil. Furthermore, the most important feature of this simulation is that the geometry can be analyzed as dipole, quadrupole or octupole windings. For the recent technology, quadrupole or octupole windings are used in FOG industry. Data set is adapted to quadrupole winding scheme as shown below.

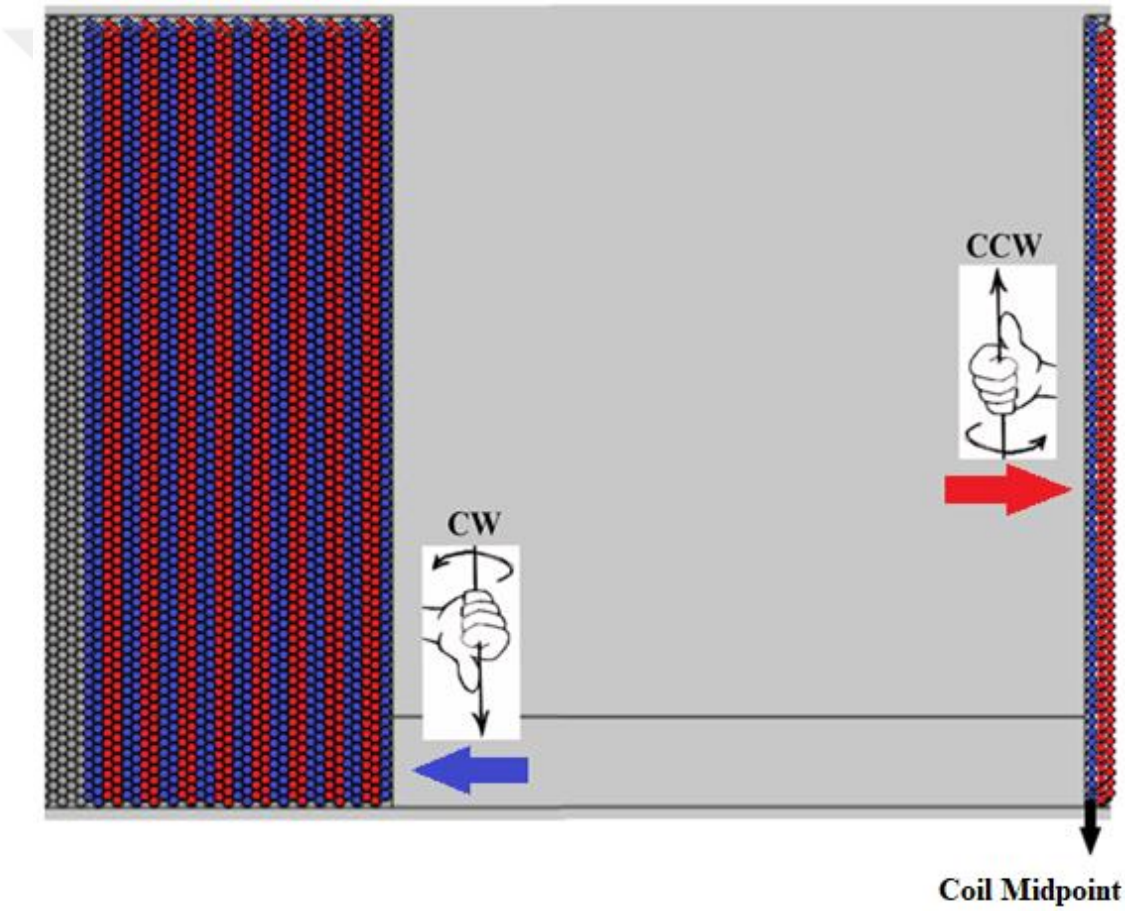

Figure 5.14 Quadrupole winding

Quadrupole winding pattern is illustrated from the patent coded US5475774 (Washington, DC: U.S Patent No. US5475774, 1995). In simulation, data set is determined as data pair which indicates two fibers next to each other. One of them carries CW beam (blue), and the other carries CCW beam (red) at the same time because they are at the same distance from the midpoint.

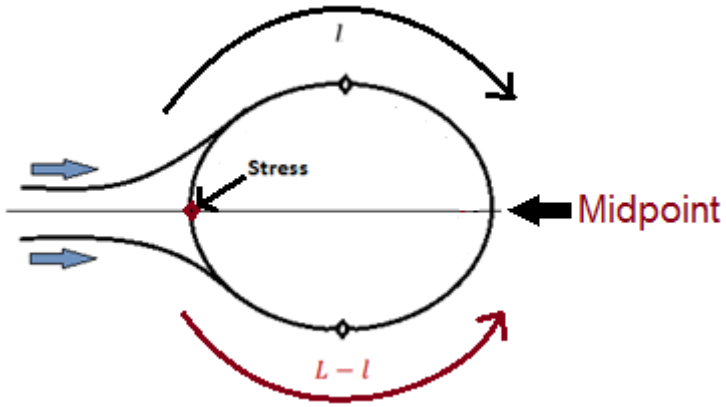

Figure 5.15 Midpoint and stress points on the cross-section of coil

In simulation, the determined stress points and midpoint is shown as an illustration in the Figure 5.15. Assuming the quadrupole winding, thermal stress points for CW and CCW light beams have equal distances as l and $L - l$ respectively from the midpoint of the coil. Data pairs are adjusted from the determined stress point with respect to the scheme of quadrupole winding.

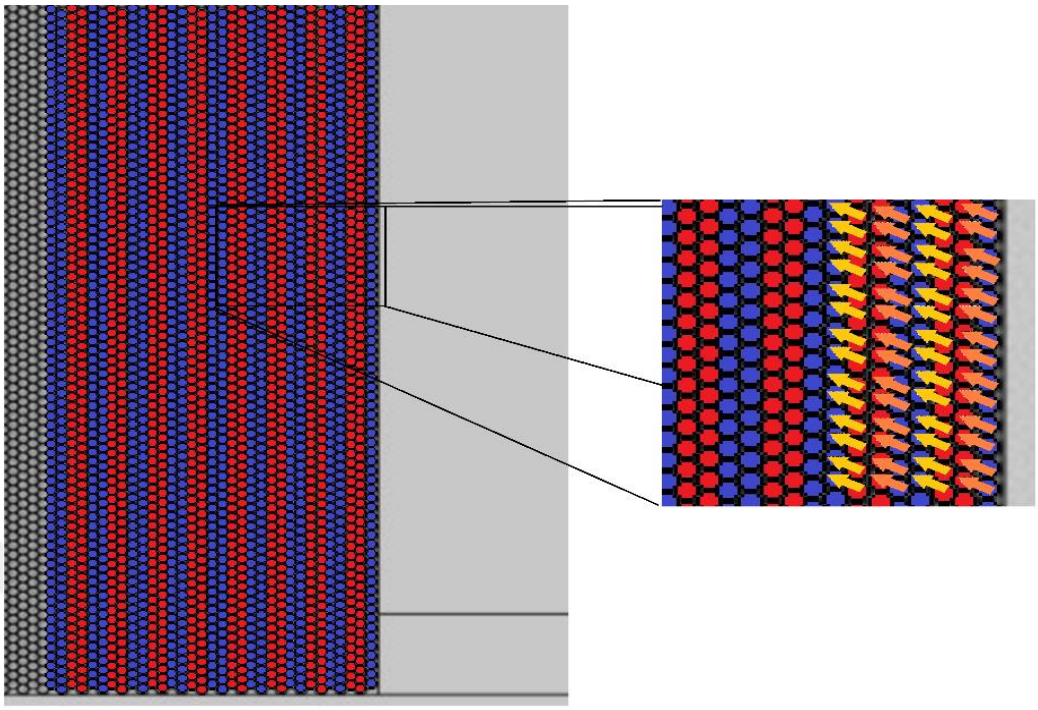

Figure 5.16 Data pair with arrows that have equal distance to midpoint of coil

Data pairs are shown in Figure 5.16. Arrows which direct blue to red fibers and red to blue fibers show the symmetric data pairs. CW and CCW beams travel these pairs at the same time because these infinitesimal lengths are assumed equidistant to the midpoint of the coil.

In simulation, the infinitesimal regions at the bottom and at the top of winding scheme are ignored for the calculations because there should be connections between them, and that is not included in the drawing.

Data sets in Comsol are selected in the left part of the coil in order to analyze them because the right and left part of the coil is totally symmetric to each other. Thus, it is enough to analyze one of them.

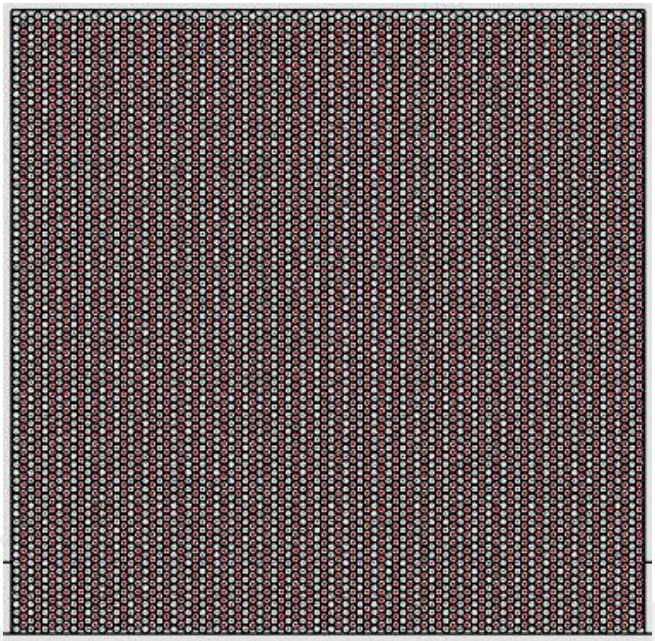

Figure 5.17 Selected points shown as red dots

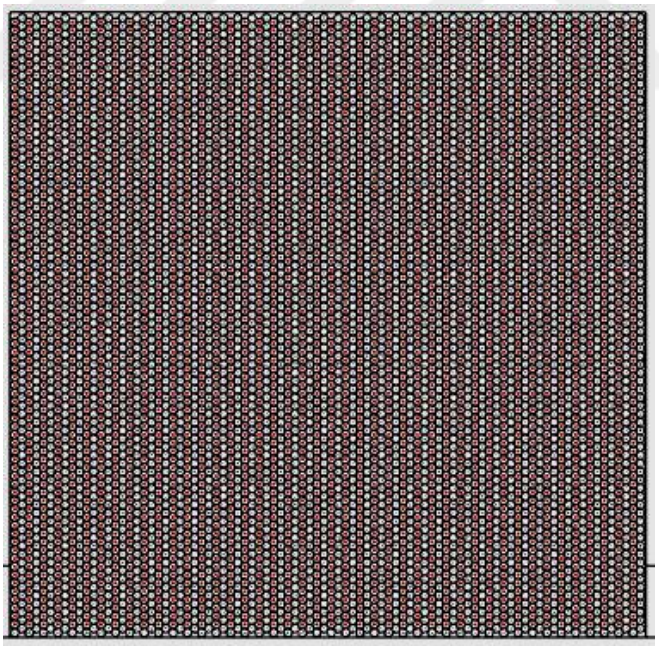

Figure 5.18 Symmetric selected points to Figure 5.17

In Figure 5.17 and Figure 5.18, the data sets are selected as shown by red dots. In Figure 5.17, data set is defined as 1st, 2nd, 3rd and up to 3256th infinitesimal length. In quadrupole winding, assuming the place of midpoint as in Figure 5.14, symmetrical infinitesimal lengths are near the selected data. Therefore, the symmetric data set is defined as 1st, 2nd, 3rd and up to 3256th infinitesimal length in Figure 5.18 as well. These are the data pairs as 1st to 1st, 2nd to 2nd and so on.

As a result, Equation 3.19 is applied in simulation, and rate error is calculated with the produced data of the thermal changes in infinitesimal lengths for every loop of the coil.

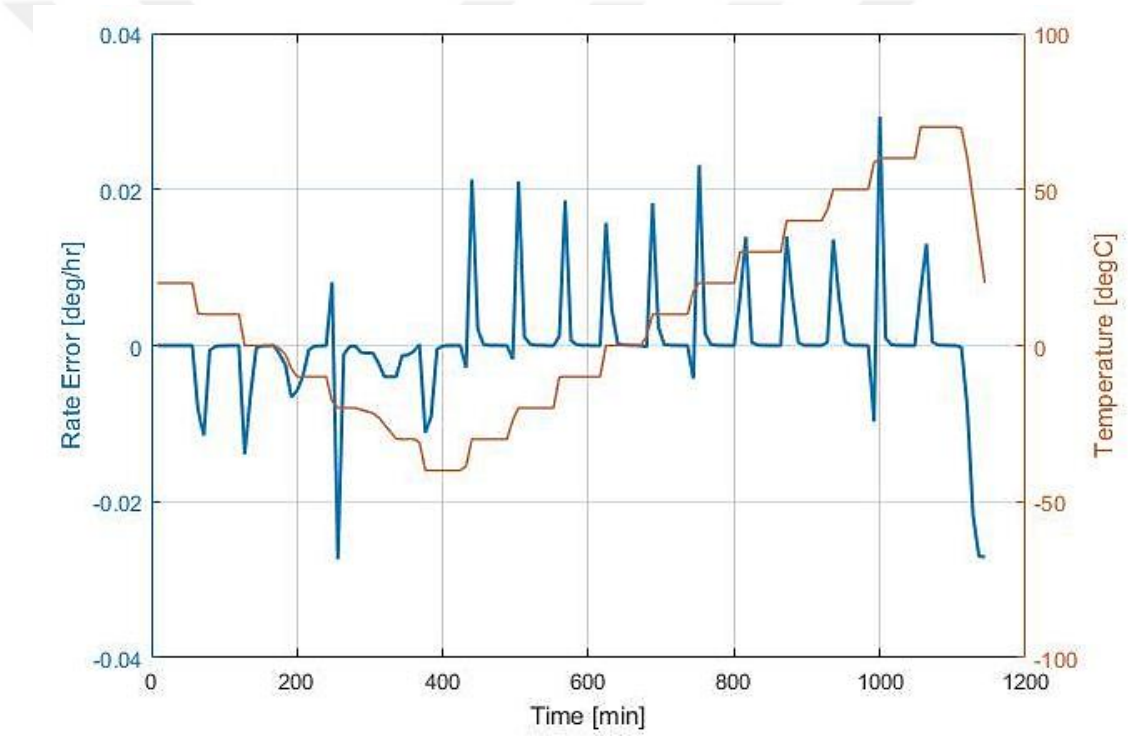

Figure 5.19 The simulation graph of rate error [deg/hr] (blue line) vs time [min] with changing temperature (orange line) for Profile 1

In Figure 5.19, rotation rate error is illustrated in blue line with respect to the thermal change in orange line at the same time. The maximum error varies in the range of

±0.02°/hr in simulation for the Temperature Profile 1. It is noticeable that there are similar peaks in Figure 4.20 as well. In the experimental data for Temperature Profile 1, rotation rate error fluctuates in the maximum range of 0.05°/hr for DSP1500 and 0.0015°/hr for DSP1750. The directions of these peaks are directly proportional to the increasing and decreasing temperatures. When the temperature is decreasing, the sign of the error is negatively grown as indicated in the Equation 3.18. Hence, the theoretical, experimental and simulation results are compatible with each other. The values of rotation rate error are not same because the result in the simulation belongs to only coil parameters, but errors from test units depends on many opto-electronic parameters. Nevertheless, they are compared to each other proportionally.

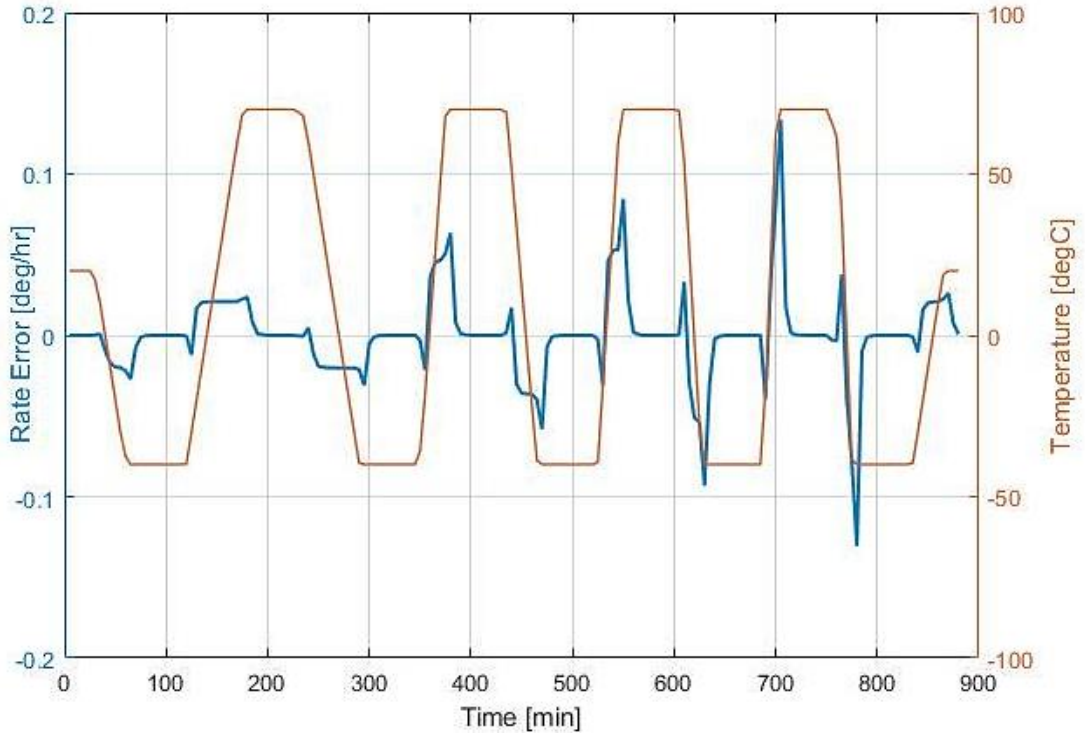

Figure 5.20 The simulation graph of rate error [deg/hr] (blue line) vs time [min] with changing temperature (orange line) for Profile 2

According to the Temperature Profile 2, it is important to notify that the shape and the behavior of the rate error shown in Figure 5.20 is similar to the graph of the test results given in Figure 4.21. Rotation rate error in Figure 5.20 is shown in blue line with respect to the change of temperature in orange line at the same time. The maximum error is distributed in the range of ±0.1°/hr in simulation for the Temperature Profile 2. This value is much more than the value given for the Temperature Profile 1. In the experimental data for Temperature Profile 2, rotation rate error fluctuates in the maximum range of 0.06°/hr for DSP1500 and 0.003°/hr for DSP1750. Moreover, as rate of thermal change is increasing, the rotation rate error also rises in Figure 5.20. This gives rise to the compatible with the theoretical result of the Equation 3.10 and experimental results in Figure 4.21.

In addition to the scheme of the previous data set, if the midpoint is selected as shown in Figure 5.21, infinitesimal fiber lengths of equal distance to the midpoint are found out from the geometry, considering the scheme of quadrupole winding.

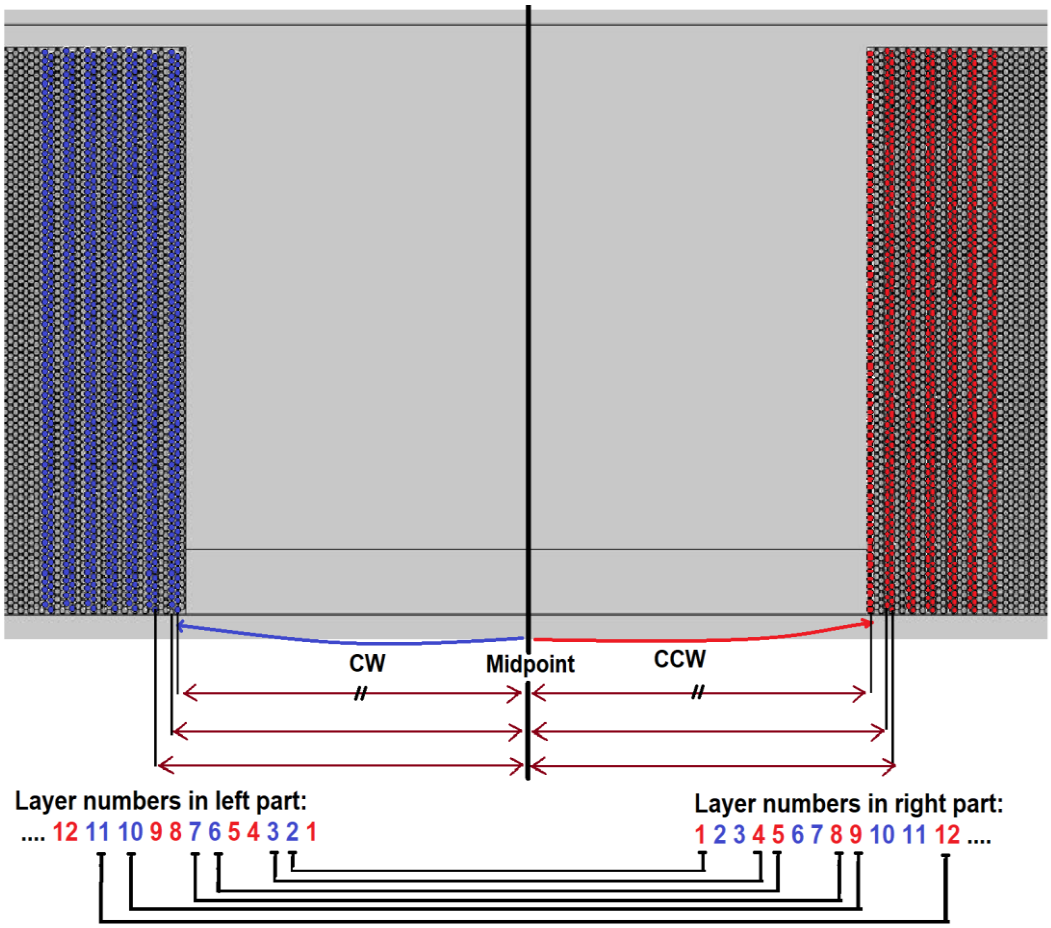

Figure 5.21 Point lenghts with equal distances to midpoint

In Figure 5.21, fibers in the matched layer numbers have approximately equal distances to the given midpoint. CW and CCW beams travel through these infinitesimal lengths of fiber at the same time. However, these point lengths are placed at the opposite ends of the coil, and they can likely be exposed to different thermal changes. Yet, in the simulation, the thermal conditions are given symmetrically from radial and axial directions. If there is an asymmetric heat transfer into the geometry, non-reciprocity arises, and rate error is resulted especially from the radial direction of coil. In the simulation, different boundary condition can be applied by considering the application.

In the symmetric thermal configuration, calculations for the rate error are the same as the simulated data, and the graphs will be obtained the same in Figure 5.19 and Figure 5.20.

In this simulation, the other winding techniques can also be studied, and data set is selected according to their configuration. The solutions can be compared with each other in order to see how their thermal dependency changes with respect to each other.

CHAPTER 6

DISCUSSION AND CONCLUSION

In this thesis, it is mentioned about the two optical gyroscopes operated by Sagnac effect: RLG and FOG. The environmental temperature change is the weak spot of these sensors. In order to perform experiments and gain simulation ability to analyze the thermal dependency of an optical gyroscope, the environmental thermal effects on fiber optic gyroscope is studied by means of theoretical, experimental and simulation approaches.

In the theoretical review, it is seen that thermal effect on a fiber optic gyroscope gives rise to serious rate errors. As an experiment, two commercial fiber optic gyroscopes are studied how their rate output is exposed to error when the thermal conditions change. However, because these products are calibrated by its firm, their residual error behaviors are examined under different temperature profiles. Besides, with the mathematical approach, simulations run for the determined temperature profiles, which are the same as the part of the experimental analysis. Considering the theoretical approach, it is expected that rate error should increase during the change in thermal conditions. However, when temperature is stable, the rate error does not change too much because the symmetrical wound coil is used in tests and assumed in simulation. The theory behind the symmetrically wound coil proves that oppositely propagated beams are exposed to the same thermal changes; therefore, they have the same defects in their refractive indices. Thus, rate errors are cancelled each other. While the environmental temperature is changing in time, symmetrically wound coil does not overcome the rate errors. Moreover, when the rate of change of temperature is higher, the rate error rises. In the test results, although the sensors are calibrated, the behavior of the residual errors are observed as the explanations in the theoretical part.

In simulation, the geometry of a quadrupole wound coil is modeled in consideration of literature (Washington, DC: U.S Patent No. US5475774, 1995), and materials and their properties are identified in this geometry. In order to observe the thermal dependency of coil materials as in the experiments, two different temperature profiles as boundary conditions are applied. After different meshes are built for every material, the simulation is run in time-dependent study. For calculations, data sets are determined. As a result of the simulation part, it can be seen that rotation rate error reacts with respect to how the temperature profiles changes. When the temperature is constant, it remains more stable around the 0 °/hr because the design of winding is assumed to be symmetrical. However, during change in temperature with respect to time, rotation rate error reacts according to the rate of change in temperature. When the rate of temperature increases, the error follows the thermal changes proportionally.

After all theoretical, experimental and simulation approaches, final data are compared between each other. These three approaches are matched and verified each other.

In this thesis, the geometry in simulation is the two-dimensional object which is the longitudinal section of a 1109-meter-long fiber coil. It can also be designed as three-dimensional object. In that case, data set should be selected for all fiber long as infinitesimal points, and the calculations should be done with these data. The more points are selected, the more realistic the result is produced from simulation.

The studied geometry of the fiber coil in the simulation can be designed in many forms in terms of a number of loop/layer, material selection, designing coil dimension and also its support dimension. Therefore, the heat can be transferred in a more symmetric way through the fiber coil. For example, if a similar aluminum support like at the bottom of the cross-section of the coil can be put at the top of the coil to spread temperature symmetrical axial directions. Hence, how the behavior of the rate error is in that boundary condition can be observed.

Moreover, symmetric winding methods are adapted to this geometry. Considering the quadrupole winding method, the numbers of the loop in the coil are counted and

selected for CW beam. Next, it is known where the CCW beam is. It is near it because the infinitesimal lengths are next to each other which have equal distance to midpoint of the coil. These points as data pairs can be selected on the geometry, depending the scheme of winding method. Therefore, the difference of refractive indices and temperature gradients between the selected points are calculated to find rate error, and also can be said that how efficient the winding is.

REFERENCES

Allan Variance: Noise Analysis for Gyroscopes. (2015). *Freescale Semiconductor APPLICATION NOTE*.

Armenise, M. N. (2014). *Advances in gyroscope technologies.* Place of publication not identified: Springer.

Benser, E., Sanders, G., Smickilas, M., Wu, J., & Strandjord, L. (2015). Development and evaluation of a navigation grade resonator fiber optic gyroscope. *2015 DGON Inertial Sensors and Systems Symposium (ISS)*. doi:10.1109/inertialsensors.2015.7314259

Bi, C., Sun, G., Wu, Y., & Zhao, K. (2011). Potted fiber optic sensor coil by novel adhesives for high-stability FOG. *International Symposium on Photoelectronic Detection and Imaging 2011: Sensor and Micromachined Optical Device Technologies*. doi:10.1117/12.898760

Claudio, C., & Tabacco, A. (2015). *Mathematical Analysis I.* Torino: Springer. Retrieved from Calculus II - Taylor Series.

Crank, J. (2011). The mathematics of diffusion. *Oxford: Univ. Pr.*

Dyott, R. (1996). Reduction of the shupe effect in fiber optic gyros; the random-wound coil. *Electron. Lett*, 32, 2177–2178.

Fang, Z. (2012). *Fundamentals of optical fiber sensors.* Hoboken, NJ: Wiley.

Fiber Optic Gyros. (n.d.). Retrieved from KVH: https://www.kvh.com/Military-and-Government/Gyros-and-Inertial-Systems-and-Compasses/Gyros-and-IMUs-and-INS/Fiber-Optic-Gyros.aspx

Global-N Temperature Cycling Chambers. (n.d.). Retrieved from https://espec.com/na/products/family/global_n

Groves, P. D. (2008). *Principle of GNSS, Inertial and Multisensor Integrated Navigation Systems.* Boston: Artect House.

Gyroscopic Effect. (2018). Retrieved from Quora: https://www.quora.com/What-is-gyroscopic-effect-How-does-it-affects-cars-planes-and-ships-Can-anyone-solve-the-mystery-of-the-rotating-flywheel-and-its-reaction-when-taking-a-left-and-right-turn

Hecht, E. (2017). *Optics.* Harlow: Pearson Education Limited.

Heimann, M., Liesegang, M., Arndt-Staufenbiel, N., Schröder, H., & Lang, K. (2013). Optical system components for navigation grade fiber optic gyroscopes. *Emerging Technologies in Security and Defence; and Quantum Security II; and Unmanned Sensor Systems X*. doi:10.1117/12.2029097

HMP4000 Power Supply Series. (n.d.). Retrieved from https://www.rohde-schwarz.com/us/home_48230.html

IEEE Standard for Sensor Performance Parameter Definitions. (n.d.). doi:10.1109/ieeestd.2014.6880296

IEEE Standard Specification Format Guide and Test Procedure for Single-Axis Interferometric Fiber Optic Gyros. (n.d.). doi:10.1109/ieeestd.1998.86153

Jin, Z., Yu, X., & Ma, H. (2013). Closed-loop resonant fiber optic gyro with an improved digital serrodyne modulation . *Optics Express*, 21(22), 26578. doi:10.1364/oe.21.026578

Korkishko, Y. N., Fedorov, V. A., Prilutskiy, V. E., Ponomarev, V. G., Fedorov, I. V., Kostritskii, S. M., & Varnakov, V. K. (2017). Highest bias stability fiber-optic gyroscope SRS-5000. *2017 DGON Inertial Sensors and Systems (ISS)*. doi:10.1109/inertialsensors.2017.8171490

Lad, P. B. (1999). Design and evaluation of an automated fiber optic untwisting machine.

Lefevre, H. C. (2014). *The Fiber Optic Gyroscope.* Boston: Artech House.

Li, X., Ling, W., He, K., Xu, Z., & Du, S. (2016). A Thermal Performance Analysis and Comparison of Fiber Coils with the D-CYL Winding and QAD Winding Methods. *Sensors*, 16(6), 900. doi:10.3390/s16060900

Li, X., Ling, W., Xu, Z., & Wei, Y. (2015). Design of a new spool for fiber coil based on the cross winding pattern. *Acta Opt. Sin.* doi:10.3788/AOS201535.0606002

Ling, W., Li, X., Yang, H., Liu, P., Xu, Z., & Wei, Y. (2016). Reduction of the Shupe effect in interferometric fiber optic gyroscopes: The double cylinder-wound coil. *Optics Communications*, 370, 62-67. doi:10.1016/j.optcom.2016.02.064

Lofts, C. M. (1995). Investigation of the effects of temporal thermal gradients in fiber optic gyroscope sensing coils . *Optical Engineering*, 34(10), 2856.

Matsumoto, H. (2006). Polarization Mode Dispersion and Its Mitigation. *Journal of The National Institute of Information and Communication Technology*, 53(2).

Mohr, F., & Schadt, F. (2008). Rigorous treatment of fiber-environmental interactions in fiber gyroscopes. *IEEE Region 8 International Conference on Computational Technologies in Electrical and Electronics Engineering*.

Mueller, H. (1937). The Theory of Photoelasticity. *American Ceramic Society*.

Mynbaev, D. K., & Scheiner, L. L. (2001). Fiber-optic communications technology. . *Upper Saddle River, NJ: Prentice Hall*.

Nayak, J. (2011). Fiber-optic gyroscopes: From design to production [Invited]. *Applied Optics*, 50(25). doi:10.1364/ao.50.00e152

Page, J. L., David, & Milliman, B. (1996). *United States of America Patent No. US5917983A.* Retrieved from https://patents.google.com/patent/US5917983A/en

Passaro, V. M., Cuccovillo, A., Vaiani, L., Carlo, M. D., & Campanella, C. E. (2017). Gyroscope Technology and Applications: A Review in the Industrial Perspective. *Sensors*, 17(10), 2284.

Pizzocaro, M. (2009). Development of a ring laser gyro: Active stabilization and sensitivity analysis.

Ponikvar, D. R., & Ezekiel, S. (1981). Stabilized single-frequency stimulated Brillouin fiber ring laser. *Optics Letters*, 6(8), 398. doi:10.1364/ol.6.000398

PXI Systems. (n.d.). Retrieved from National Instruments: http://www.ni.com/en-tr/shop/pxi.html

Randy, P., & Ralph, A. B. (1995). *Washington, DC: U.S Patent No. US5475774.*

Ring laser gyroscope. (n.d.). Retrieved from Britannica: https://www.britannica.com/technology/ring-laser-gyroscope

Saleh, B. E., & Teich, M. C. (2009). *Fundamentals of photonics.* Hoboken, NJ: Wiley-Interscience.

Sardinha, M., Rivera, J., Kaliszek, A., & Kopacz, S. (2007). *United States of America Patent No. US20090141284A1*. Retrieved from https://patents.google.com/patent/US20090141284A1/en

Shamir, A. (2006). An Overall of Optical Gyroscopes Theory, Practical Aspects, Applications and Future Trends.

Shupe, D. M. (1980). Thermally Induced Non-reciprocity in the Fiber-Optic Interferometer. *Appl. Opt.*, 654-655.

Titterton, D., & Weston, J. (2004). *Strapdown Inertial Navigation Technology*. Stevenage: IET.

Wang, Z., Ju, J., & Jin, W. (2005). Properties of elliptical-core two-mode fiber. *Optics Express*, 13(11), 4350. doi:10.1364/opex.13.004350

Woodman, O. J. (2007). An Introduction to Inertial Navigation. Strapdown Inertial Navigation Technology. 1-37.

Xiong, W. (2010). *Applications of Comsol Multiphysics Software To Heat Transfer Processes.* Helsinki.

Yi, X., & Wen, X. (2006). Y-integrated optic chip (Y-IOC) applied in fiber optic gyro. doi:10.1117/12.693438

Yong, W. Z., Qi, Q., & Jin, S. S. (2014). Temperature dependence of the refractive index of optical fibers. *Chin. Phys. B*, 23(3).

Zhang, Y., Gao, Z., Wang, G., & Gao, W. (2014). Modeling of Thermal-Induced Rate Error for FOG With Temperature Ranging From -40 °C to 60 °C. *IEEE Photonics Technology Letters*, 26(1) 18-21. doi:10.1109/lpt.2013.2288631

Zhang, Z., & Yu, F. (2017). Quantitative analysis for the effect of the thermal physical property parameter of adhesive on the thermal performance of the quadrupolar fiber coil. *Optics Express*, 25(24), 30513.